Air Force Office of Scientific Resarch
under Grant F49620-95-1-0132

CLOUD-RESOLVING SIMULATIONS OF TROPICAL CIRRUS CLOUDS

by Cristian Mitrescu

William R. Cotton, P.I.

Colorado State University

DEPARTMENT OF ATMOSPHERIC SCIENCE

PAPER NO. 654

CLOUD–RESOLVING SIMULATIONS OF TROPICAL CIRRUS CLOUDS

by

Cristian Mitrescu

Department of Atmospheric Science

Colorado State University

Fort Collins, CO 80523

Air Force Office of Scientific Research

under Grant F49620–95–1–0132

April 30, 1998

Atmospheric Science Paper No. 654

ABSTRACT

CLOUD–RESOLVING SIMULATIONS OF TROPICAL CIRRUS CLOUDS

Since up to 20% of the Tropics is covered by cirrus clouds, it is expected that they strongly influence the atmospheric radiative balance and the thermal equilibrium of the Earth through their complex microphysical structure.

Two–dimensional and three–dimensional simulations of a cirrus cloud event over the Western Pacific during TOGA COARE were performed using RAMS in an LES configuration.

Both simulations showed the formation of two layers separated by a dry layer. In the top layer pristine ice was the dominant feature while in the bottom one mostly aggregates were present. The two layers proved to be coupled in the presence of internal stratification. Mixing ratios for the hydrometeors (only pristine ice, snow, aggregates and cloud droplets were allowed) and the vertical profiles are consistent with measurements. Within these two layers a layered structure and a horizontal variability is observed.

Like other studies and measurements it is showed that the nature of turbulence in cirrus clouds is two–dimensional and buoyancy is the main source.

Heating rates, which are responsible for inducing convection that is important in the maintenance of cirrus clouds, computed with the new radiation scheme, are about -17 K/day which is consistent with other models.

Since one of the goals of the TOGA COARE is to determine new parameterizations that can be used in single–column models, the Probability Distribution Function for vertical velocity was computed and approximated with a Gaussian function. This can be latter used when computing various terms that depend on speed in the microphysical module.

Cristian Mitrescu
Department of Atmospheric Science
Colorado State University
Fort Collins, Colorado 80523
Summer 1998

ACKNOWLEDGEMENTS

I would first like to thank my adviser, Dr. William R. Cotton, for giving me the opportunity to work with RAMS and for the support and guidance he has given me in my research. I would also like to thank my committee members Dr. Graeme L. Stephens and Dr. Chiaoyao She for taking time to review this thesis.

Special thanks to all the members of Cotton's group, but special thanks to Bob Walko, Jerry Harrington, Ting Wu, Hongli Jiang, Brian Gaudet and Chris Golaz for their constant support and help.

A big thank you for Brenda Thompson, Abby Hodges and Connie Uliasz for their assistance in administrative work, while John Blanco and Dave McClure helped me whenever my computer knowledge was too low.

I would like to thank my family for always being "here" even though they are miles away. And I would like to give thanks to God, for making all things possible.

This research was supported by the Air Force Office of Scientific research under grant # F49620–95–1–0132.

TABLE OF CONTENTS

LIST OF FIGURES

LIST OF TABLES

Chapter 1

INTRODUCTION

One of the major uncertainties in global climate prediction is due to the use of simple parameterizations of clouds. The use of explicit cloud parameterization instead of diagnostic schemes can improve the uncertainty. Also as models and observational techniques become more sophisticated, it is necessary to validate them using quantities that are more fundamental and are averaged over smaller spatial and time scales.

Cirrus clouds are relatively stable and long–lived and are mostly associated with large–scale disturbances, being present in all latitudes and without respect to land or sea or season. They have a significant impact on the atmosphere through their radiative effects and therefore modulate atmospheric systems on many time and space scales. They may also have an important role in developing precipitation in many mesoscale and large–scale atmospheric systems. Tropical cirrus anvils, formed by deep convective activity, are thought to play a crucial role in determining the Earth's radiation budget and climate; they also account for most of the cloud cover over tropical oceans. Besides marine stratocumulus and their strong albedo effect, cirrus clouds regulate sea surface temperature and subsequent convective activity. Since they exist in the coldest part of the troposphere directly over the warm ocean they produce the strongest greenhouse effect.

Thin cirrus clouds cause a significant warming of the equilibrium climate, particularly in the tropics. In contrast, clouds of higher optical depths, such as deep convective clouds, deep frontal clouds and boundary–layer stratus, can cause an appreciable cooling (*Cess et al., 1990, Stephens and Greenwald, 1991*). Equatorial cirrus are the coldest class of tropospheric clouds on the planet and are found over the world's warmest waters. They therefore have the potential to cause the greatest warming of the equilibrium climate by cloud–radiation interactions (*Ramaswamy and Ramanathan, 1989*). Equatorial cirrus tend to be associated more with deep moist layers. They also have higher emittance values than those in the mid–latitude which is likely to be due to the deeper clouds that exist in the tropics.

Recent General Circulation Models (GCMs) predict an increase in optical depths of cirrus clouds with global warming (*Roeckner, 1988*). Thus a knowledge of the optical properties of cirrus clouds is crucial for prediction of future climates. The significance of tropical cirrus clouds has been highlighted through their possible control of the sea surface temperature in the Tropical West Pacific (*Ramanathan and Collins, 1991*). The temperature and stability of the atmosphere containing cirrus clouds will similarly be affected (*Arking and Ziskin, 1994*). *Prabhakara et al. (1991)* have detected extensive sheets of thin cirrus covering tropical regions, particularly the Tropical West Pacific.

Tropical cirrus can also induce circulations in the vertical as a result of IR heating near cloud base and IR cooling near cloud top (*Lilly, 1988*) and can modify the water vapor concentration in the upper troposphere and lower stratosphere (*Danielsen, 1982*).

In order to better understand the role of cirrus clouds in the atmosphere, many models have been proposed to describe the growth, maintenance and decay phases of the cirrus cloud life cycle. Due to the high complexity of the cirrus clouds this is only possible with high resolution, explicit microphysical models and accurate radiation schemes. But when developing a (complex) model as for cirrus cloud, even if treated with detailed microphysics, it may still fail to accurately represent real clouds for (at least) three reasons:

- the initial conditions may not be accurate

- sub–grid–scale dynamics may dominate the cloud processes
- our knowledge of cirrus microphysics may be too rudimentary to allow a realistic simulation.

The aim of this thesis is to simulate the dynamics of tropical cirrus clouds using the Regional Atmospheric Modeling System (RAMS) set as a three–dimensional model in a Large Eddy Simulation (LES) configuration. Specifically we simulate over the region and during the time when the Tropical Oceanic Global Atmosphere Coupled Ocean Atmosphere Response Experiment (TOGA COARE) took place. It uses data from a previous run of the same RAMS set as a two–dimensional Cloud Resolving Model (CRM). These data are used as an initial set as well as for nudging. RAMS is an ideal tool for simulating cirrus clouds. It has a complete radiation parameterization, a bulk microphysical parameterization and has the capability of specifying the vertical grids.

Chapter two provides background information about cirrus clouds along with some previous studies.

In chapter three the RAMS model as used in this simulation is described. Main objectives of the TOGA COARE are described in chapter four.

Chapter five concentrates on the case study: a simulation during the TOGA COARE experiment.

Summary and conclusions as well as some suggestion for future research are addressed in chapter six.

Chapter 2

PREVIOUS WORK

2.1 Introduction

Many similarities can be pointed out between cirrus clouds and stratocumulus clouds. Both types of clouds are fairly dynamically inert, in a synoptic sense, and have large horizontal dimensions. There is a complex balance involving radiational effects, turbulence, and microphysical interactions that describe the internal processes in these clouds. They both often have a well mixed region and are usually composed of several layers. At their top an inversion is present: for stratocumulus due to subsidence and for cirrus due to the tropopause. But yet the cirrus clouds are more complex with regard to their microphysical structure: ice and liquid water can coexist and the processes are more complex. Cirrus often form in regions of widespread ascent while stratocumulus form in regions of widespread descent. Moreover, unlike low– and middle–level clouds that consist of water with large optical thickness, and therefore treated as blackbodies, high level cirrus clouds consisting of large amounts of nonspherical ice particles, are normally thin and nonblack. Both numerical models and measurements have proven that the influence of optically–thin and nonblack cirrus on the radiation budget and on the weather and climate depends on both solar and infrared radiative properties.

Weickmann (1945, 1947) was the first to measure the composition of cirrus clouds. He measured a mean crystal length of 100–300 μm and an ice content of approximately 0.01 gm^{-3}. The predominant particle habit was columns and bundle of columns. Heymsfield and Knollenberg (1972), and Hobbs et al. (1975) measured the mean crystal length as 60–1000 μm with an ice content of 0.006 to 0.3 gm^{-3} and the predominant particle habit as columns, bullet, rosettes and plates. An aircraft–derived composition and structure of cirrus clouds and a summary of equipment used for in–situ sampling are presented in Table 2.1 and Table 2.2 respectively. In the Table 2.1 L is the mean crystal length, T is temperature and IWC is the ice water content.

Table 2.1: Aircraft observations of the composition and structure of cirrus clouds. After *Liou (1986)*

Investigator	Cloud Type	Synoptic structure	Composition
Weickmann (1945,1949)	cirrocumulus, cirrostratus	—	column, bundle of columns $L \sim$ 100–300 μm $IWC \sim$ 0.01 gm^{-3}
Heymsfield, Knollenberg (1972)	cirrus uncinus, cirrostratus, anvil	—	bullet rosette, column, plate $L \sim$ 600–1000 μm $IWC \sim$ 0.15–0.25 gm^{-3}
Hobbs et al. (1975)	cirrus, cirrostratus	upper level trough, frontal system	bullet, column, plate $L \sim$ 100–700 μm $IWC \sim$ 0.01–0.1 gm^{-3}
Heymsfield (1975)	cirrus uncinus cirrostratus	$T \sim$ -19:-58°C, strong wind shear	bullet rosette, column, plate $L \sim$ 20–2000 μm $IWC \sim$ 0.15–3 gm^{-3} $L \sim$ 20–500 μm $IWC \sim$ 0.01–0.15 gm^{-3}
Heymsfield (1977)	stratiform ice clouds	$T \sim$ -10:-60°C, frontal system, jet stream	bullet rosette, column, thick plate $L \sim$ 300–600 μm $IWC \sim$ 0.001–1 gm^{-3}
Varley et al. (1978-1980)	thin cirrus, cirrostratus	upper level trough high pressure system	bullet rosette, column, plate $L \sim$ 20–2000 μm $IWC \sim$ 0.001–0.05 gm^{-3}

A general description of the composition and structure of extra–tropical cirrus clouds is:

- there are several types of cirrus clouds, including thin cirrus and contrails, cirrostratus, and cirrus uncinus;
- their base heights in the earth's atmosphere vary greatly with respect to season and location, but generally range from 4 to 15 km and have a base temperature of $-20°C$
- cirrus clouds are composed predominantly of bullets, columns, and plates;
- the IWCs for various types of cirrus clouds has been described by the following equation (*Heymsfield and Platt, 1984*) when $T < -20°C$:

$$ln(IWC) = -7.6 + 4 \cdot exp[0.2443 \times 10^{-3}(T + 20)^{2.455}] \tag{2.1}$$

- a majority of ice crystals in cirrus clouds seem to be horizontally oriented with their longer axes parallel to the ground;
- the aspect ratio of bullets and columns in cirrus may be defined by equations (*Heymsfield, 1972*):

$$d_{bullets} = \begin{cases} 0.25L_b^{0.79} & L_b \leq 0.3 \text{ mm} \\ 0.19L_b^{0.53} & L_b > 0.3 \text{ mm} \end{cases} \tag{2.2}$$

$$d_{column} = \begin{cases} 0.5L_c & L_c \leq 0.3 \text{ mm} \\ 0.2L_c^{0.41} & L_c > 0.3 \text{ mm} \end{cases} \tag{2.3}$$

- cirrus (< 1km) and cirrostratus are probably associated with either high pressure systems or upper level troughs. Cirrus uncinus are related to either mesoscale or large-scale synoptic flows.

The magnitude of the vertical motions in cirrus depend on the type of cirrus; warm frontal cirrus clouds are characterized by vertical motions of the order of 1–10 cm/s, warm front occlusions by 20 cm/s, and convective elements near the jet stream exhibit vertical motions of the order 50–70 cm/s (*Heymsfield, 1975*).

Table 2.2: Equipment used for in–situ sampling of quantities related to cloud microphysics. After *McFarquhar and Heymsfield (1996a)*

Instrument	Quantity Measured	Measuring Range	Accuracy/ Resolution	Data Quality
PMS 2DC	shadows of particle images & particle sizes	30 to > 1800 μm	30 μm photodiode; higher threshold at high air speeds	very good; resolution degraded due to high speeds
PMS 2DP	shadows of particle images & particle sizes	120 to 6000 μm	120 μm photodiode	stuck bit on some missions; fast air speeds make data recovery difficult
FSSP-300	forward scattering of light from particles	0.6 to 21 μm	19 size bins from 31 to limit scattering ambiguities	unknown effects due to non-sphericity of ice and interference from larger crystals
VIPS	images of crystals collected on tape and video	approx. 5 to 150 μm	resolution of 5 μm	quality of focusing varies between days; becomes saturated with crystals images at large IWCs (0.05 gm^{-3})
Rosemount temperature probe	ambient temperature	all flight ranges	$\pm$ 0.5°C	speed runs helped calibration

Two–dimensional turbulence (*Flatau et al., 1990*) may characterize the turbulence for most of the cirrus. This is supported by measurements that showed that the vertical velocity variance is an order of magnitude less than the horizontal variance (*Quante, 1989*). In this case the energy does not cascade to smaller scales, but it propagates to larger scales. This two–dimensional turbulence can be related to cirrus in the following way: small scale turbulence becomes quasi two–dimensional under stable stratification, quasi two–dimensional turbulence is persistent as dissipation is small, vertical motions are suppressed compared to horizontal; the cloud shrinks vertically and becomes thin; motions in individual layers are decoupled. Measurements by *Smith et al. (1990)* and *Sassen et al. (1989)* showed a jump in variance measured at all levels at the 5 km wavelength suggesting a dominant source of energy at this scale. *Quante (1989)*, using aircraft data, concluded that turbulence was due to wind shear and the breaking of Kelvin–Helmholtz waves. It was also inferred that more turbulence was produced in the lower part of the cloud, while shorter wavelength waves were at the top of the cloud.

2.2 Cirrus size spectra

In order to better simulate the life–cycle of a cirrus cloud, knowledge about the structure of the hydrometeor size spectra is required. To do that, direct sampling using high–altitude aircraft and remote sensing techniques by ground–based and airborne–systems are used. However, the basis functions deduced and used in models to describe cirrus cloud behavior and properties are often highly simplified and the potential influences on cirrus properties caused by climate changes are poorly understood.

Heymsfield and Platt (1984) showed that both the form of the size distributions and crystal habits changed systematically with temperature, with the largest change occurring between -40 and -50°C (valid for mid–latitude cirrus). The shape of the tropical size distributions substantially differ from those of mid–latitude size distributions, especially at temperatures lower than -40°C and there are more small crystals than for mid–latitude cirrus (*Heymsfield and McFarquhar, 1996)*. Also the crystal types are very different than those in mid–latitude cirrus produced by synoptic scale lifting: more pronounced shape features at each height level and many clearly defined bullet rosettes. For tropical cirrus bullet rosettes were very rare. Sub–50 μm particles often have non–spherical shapes, and columns, although infrequently observed, tend to occur most often in regions of low IWC. By contrast, distinct columnar shapes including bullet rosettes are the dominant shapes found in mid–latitude, non–thunderstorm–generated cirrus.

The new parameterization that *McFarquhar and Heymsfield (1996b)* introduce to describe the size spectra for tropical cirrus clouds has the properties that:

- 1. optical and radiative properties from the parameterized size distribution replicate those from the observed size distribution as close as possible;
- 2. mass is conserved;
- 3. the contribution of the smaller ice crystals is representative;
- 4. is easily integrable over all sizes.

and it depends on mass–equivalent dimension (D_m):

- for small ice crystals (the size spectra is best fit with a gamma function):

$$N(D_m) = \frac{IWC_{<100}\alpha^5_{<100}D_m}{\pi\rho_{ice}\Gamma(5)}exp(-\alpha_{<100}D_m) \tag{2.4}$$

- for large crystals (the size spectra is best fit with a lognormal function):

$$\begin{aligned} N(D_m) &= \frac{6IWC_{<100}}{\pi^{3/2}\rho_{ice}\sqrt{2}exp(3\mu_{>100}+\frac{9}{2\sigma^2_{>100}})D_m\sigma_{>100}} \\ &\cdot exp\left[-\frac{1}{2}\left(\frac{logD_m-\mu_{>100}}{\sigma_{>100}}\right)^2\right] \end{aligned} \tag{2.5}$$

The subscript 100 emphasizes that those distributions are designated for crystals smaller (small crystals case) or greater (large crystals case) than 100 μm. Here $\alpha_{<100}$ is a parameter of the first order gamma distribution, $\sigma_{>100}$ is the geometric standard deviation of the distribution, $\mu_{>100}$ is the location of the mode, $IWC_{>100}/IWC_{<100}$ is the mass of all crystals greater/smaller than 100 μm.

Although an exponential distribution provided a marginally better fit statistically to small ice crystal spectra, the gamma distribution was used due to the fact that its number distribution function approaches zero at zero diameter. Both functions can be applied for the whole domain because the number distribution is smaller when the diameter is outside the range. From the data the authors proposed the following dependencies:

$$IWC_{<100} = a\left(\frac{IWC}{IWC_0}\right)^b \tag{2.6}$$

where $a = 0.252 \pm 0.068$ gm^{-3} , $b = 0.837 \pm 0.054$ and $IWC_0 = 1$ gm^{-3}.

$$\alpha_{<100} = b - m\,log\left(\frac{IWC_{<100}}{IWC_0}\right) \tag{2.7}$$

where $b = -4.99 \times 10^{-3} \pm 5.50 \times 10^{-3}$ μm^{-1} and $m = 0.0494 \pm 0.0029$ μm^{-1}.

In the same way the authors propose the following dependencies:

$$\mu_{>100} = a_\mu(T) + b_\mu(T)\left(\frac{IWC_{>100}}{IWC_0}\right) \tag{2.8}$$

$$\sigma_{>100} = a_\sigma(T) + b_\sigma(T)\left(\frac{IWC_{>100}}{IWC_0}\right) \tag{2.9}$$

where $a_\mu, b_\mu, a_\sigma, b_\sigma$ are linear functions of temperature. From the data the conclusion is that the mode shifts to larger values for larger IWCs and warmer temperatures. This is consistent with previous observations showing larger and broader size distributions at higher IWCs and higher temperatures.

The goal of this new parameterization is to characterize the radiative effects of tropical ice crystals size distribution given the ice water content (IWC) and temperature (T). Hence, given any T and IWC, the size distribution can be computed using the parameterization.

This parameterization is consistent with previous studies that have suggested that there may be two peaks in the distribution functions of ice crystals. When plotting mass distribution function, two peaks, corresponding to the large and small ice crystals, are seen at diameters of approximately 50 and 200 μm for IWCs between 10^{-1} and 10^{-3} gm^{-3}. The 200 μm peak location would roughly correspond to a 300 μm peak location for maximum crystal length, which is consistent with previous observations of cirrus. It has also been inferred from the study that the assumed major role played by small ice crystals is not true: crystals with dimensions smaller than 20 μm do not contribute substantially to the optical properties of cirrus as calculated using the radiative transfer code of CCM2. But this could be due to the limitations of the code rather than physical factors. Another finding was that quasi–circular and hexagonal platelike crystals are the most common shapes for smaller crystals and the particle habits differ significantly from those observed in midlatitude cirrus (bullet rosettes); aggregates were especially seen when IWC was higher; also the horizontal distribution is more inhomogeneous.

Lidar measurements in the tropical cirrus suggest the presence of either supercooled drops or horizontal ice crystal plates *(Platt, 1978)*. The profile of humidity indicates values below ice saturation, thus suggesting the latter. However, the humidity data may have systematic errors, so their conclusions are only tentative.

2.3 Radiation

To a first approximation the bulk cloud radiative properties are determined by the size distribution of hydrometeors. Radiative properties of cirrus clouds are very sensitive to the environmental conditions in which they form. The temperature of the cloud environment and the height of the cloud above the surface have a great influence on their radiative properties especially in the IR region. During the *Barbados Oceanographic and Meteorological Experiment* large variabilities in emission and albedo have been found: absorption 13–40 %, reflection: 47–59 % (*Reynolds et al., 1975*).

Heymsfield and Miloshevich (1991) suggested that ice crystals with dimensions smaller than 25 μm can substantially contribute to increasing cloud albedo. This hypothesis was also confirmed by *Stephens et al. (1990)* based on Mie Theory calculations. However *Pueschel et al. (1995)* found that it is the aerosol that is mostly responsible for the upscattering of solar radiation. But their analysis may be not true since their data was collected using a 2D Grey scale probe that are inaccurate for measuring crystals smaller than 100 μm.

A model with high resolution microphysics is required in order to correctly simulate the radiative budgets of cirrus as the size distributions changes throughout the growth, maintenance and decay phases of a cirrus life cycle.

In a two–stream model proposed by *Stackhouse and Stephens (1990)* a 3-km thick uniform cloud layer is first analyzed in a tropical region and then in a sub–arctic winter region. The profiles show enhanced cloud–top IR cooling and solar heating and an enhanced cloud-base IR heating, which increases as IWC increases. The IR budget of the cirrus is governed by the difference in the temperatures of the cloud and the temperature below the cloud. A conclusion is that the longwave radiative heating and cooling depends on the amount of ice, the temperature difference between the cloud and the surface below, and the characteristics of the atmosphere. It was also inferred that the LW radiation budget depends on altitude - flux divergence for low cirrus and net flux convergence for high cirrus - and the SW heating rates vary with the cloud ice content and altitude.

Zender and Kiehl (1994), using a one–dimensional model found that a small change in the absorption properties of a given distribution of condensate can result in significant changes in local rates as the optically–thick clouds are characterized by sharp changes in flux profiles and as crystals smaller than 20 μm are also highly efficient absorbers in the LW region. In the SW region, the importance of small crystals is revealed by the fact that Mie theory absorption efficiency for ice spheres exhibits a peak at $\lambda = 3$ μm for crystals sizes $1 < r < 8$ μm and depends mostly on the refraction index and size parameter.

Toon et al. (1989) who developed the NASA/ARC two–stream radiative transfer code, divided the solar and infrared spectral regions into 26 and 18 spectral intervals, respectively. This allows direct comparison of the simulated fluxes and intensities with spectral measurements. Absorption by atmospheric gases is treated with exponential fitting and it accounts for molecular absorption, infrared continuum absorption by water vapor, absorption and scattering by liquid water or ice cloud particles - which are defined for each spectral interval by the three single–scattering properties: volume extinction coefficient β_e, the single–scattering albedo ω_0, and the asymmetry parameter g. These quantities are expressed in terms of water content and effective radius r_e and thus eliminates the need for explicit integrations over particle size. The infrared extinction is corrected to compensate for the large infrared extinction of smaller ice crystal sizes:

$$\beta_{eIR} = 10^3 IWC(0.00413 + \frac{2.92}{r_e})(1.03 + \frac{2.73}{r_e}) \quad , \text{(in km)}. \tag{2.10}$$

For water clouds the extinction coefficient is computed using an extinction cross–section of 2 (and assumed to apply at all wavelengths):

$$\beta_e = \frac{3 \times 10^3 LWC}{2\rho r_e} \quad \text{(in km)} \tag{2.11}$$

and the single scatter albedo (for both ice and water clouds at all wavelengths) the estimate is:

$$\omega_0 = 0.5 + 0.5\, exp(-2k_\lambda r_e) \tag{2.12}$$

where $k_\lambda = 4\pi n_i/\lambda$. Since for thermal wavelengths scattering is less important and therefore the non–sphericity of the crystals can be neglected a value for g can be set: $g = 0.87$ for cloud and $g = 0.9$ for ice. For water clouds a value of 10 μm for r_e is a good approximation. For ice clouds, the value for r_e is proposed from FIRE–I and FIRE–II data:

$$r_e = \begin{cases} 30 + 1.2(50 + T)[4 + log(IWC)] & ,T > \text{-50°C and} \\ & IWC > 10^{-4}\ \text{gm}^{-3} \\ 30 & \text{,elsewhere.} \end{cases} \tag{2.13}$$

This expression for effective radius (in μm) as a function of both temperature (T) and ice water content (IWC) provides a better fit than the expression involving temperature or ice water content alone. When interpolating (to the dynamical grid) the layered structure of the cirrus is eliminated and smoothed profiles result. Although this simplified model uses the approximation of bulk optical properties and an explicit size distribution, these two approximations are adequate as evidenced by the fact that computed parameters are very close to those computed from detailed Size–Resolving Model. The differences between the observed and predicted radiative quantities are due to errors in the prediction of ice water content, and not due to the optical properties or the solution technique.

Using a two–dimensional Eulerian model to simulate cirrus clouds, *Starr and Cox (1985)* obtained realistic results for ice water content and vertical motions. The horizontal scale between convective cells and the layering tendency was also simulated. In a second set of simulations, they concluded that radiation plays an important role in modulation of local buoyancy; that large scale ascent or descent is critical in determining the physical properties of the cloud; the fact that changing the crystal fall speed affects the physical properties of the cloud.

Fleming and Cox (1974) and *Roewe and Liou (1978)* showed that cirrus clouds strongly suppress tropospheric cooling and significantly increase cooling in the stratosphere above 20 kilometers and the presence of low–level clouds significantly modifies the cooling within the cirrus cloud. Based on theoretical calculations, cirrus clouds will generate a significant vertical and horizontal inhomogeneity with respect to heating rates. This will affect the dynamic processes and therefore the temperature distribution. Still unknown is the role (mechanism) that cirrus clouds play in the energy exchange between the troposphere and stratosphere.

Comparisons made between the heating rates and surface fluxes calculated with the radiative model and those computed using a two–stream size–resolving radiation model (which explicitly calculates optical properties for ice crystal size distribution based on Mie theory and corrections for irregularly shaped particles) showed that the differences were small (within the error associated with the approximations to r_e and IWC).

The higher emittance of tropical–cirrus clouds compared to mid–latitude cirrus is explained to be due to deeper clouds in the tropics. But computed values for the infrared absorption coefficient σ_a were similar to those for mid–latitude cirrus, leading to the idea of a useful parameterization, as well as validation, for climate models (*Platt et al., 1997*).

2.4 Microphysics

The modeling of cirrus clouds, due to their high complexity, is a difficult task. Cirrus clouds are characterized by a wide range of values for crystal habit, crystal diameter and IWC. From the observed crystal habits, possible processes can be inferred: bullet rosettes are due to freezing at water saturation; rosettes develop in clouds with relatively large vertical motions; plates and columns are found in less vigorous clouds due to deposition at low ice supersaturation.

When developing a scheme to describe the microphysical properties and its influence on cloud dynamics and thermodynamics several simplifications have to be made in order to lower the computing time and memory needed for such a task. But the principal aspects must be well described. To do that, precise measurements - in–situ or labs - have to be performed. This will provide data to derive empirical formulas regarding mass–diameter relations, fall speed expressions, crystal habits dependencies, along with a better understanding regarding physical and chemical processes that take place in a cirrus clouds.

In a model by *Toon et al. (1989)* the microphysical treatment was to consider various conversion mechanisms between different aerosols types and water vapor. Sensitivity tests showed that: the total number of CN present in the upper troposphere has little or no effect - the number of ice crystals which nucleate depends primarily upon the temperature at which the nucleation occurs and the cooling rate; the magnitude of vertical motion controls the cooling rate and the supply of water; therefore, this can affect ice crystal number density, ice water content, cloud albedo, cloud optical depth, and cloud radiative forcing. Cloud height sensitivity tests showed trends of increasing ice number density, decreasing effective radius, decreasing ice content, and increasing net radiative forcing with increasing cloud height.

The aerosol content in the atmosphere, along with cloud dynamics regulate the particle size distribution in cirrus clouds. This is done through two fundamentally different processes for ice formation: homogeneous freezing of clouds droplets and haze particles (CCN) and heterogeneous nucleation on ice nuclei (IN). *DeMott et al. (1994)* used a microphysical parcel model and a mesoscale cloud model to investigate the impact of these two processes on the formation of cirrus clouds. The homogeneous nucleation alone produces more pristine ice crystals that grow more slowly and have longer residence times at higher altitudes in the cloud than the heterogeneous case. It is pointed out the critical nature of the vertical structure of the heterogeneous ice nuclei concentrations that, even in small concentrations, can greatly reduce ice crystals concentrations, and lower the required humidity for cloud formation. The sensitivity tests showed that a large increase in large CCN does not greatly affect the ice crystal concentration, but allows the formation of cirrus clouds at lower humidities (2 % lower). Large injections of IN have the result that the clouds form more easily and contain fewer and larger ice particles. Another finding was that very high ice crystal concentrations are formed in strong vertical motions of orographic wave clouds. Since homogeneous ice formation is sensitive to small changes in the humidity profile, the need of better resolution and data are required in order to better simulate the ice crystal structure in cirrus clouds.

Petch et al. (1997) used a simple column model to investigate how different bulk microphysical schemes influence hydrometeor contents and radiative heating rates in a cloud. Sensitivity tests showed that the assumption that ice crystals have a zero fall speed plays a major role in a dissipating cirrus: very little ice is removed in contrast to almost complete dissipation for the case when a non zero fall speed is assumed. Another effect is that when allowing the ice crystals to fall the cloud becomes less well defined. That reduces the cooling rates. Also the infrared radiation has a larger effect in the case when the ice contents are lower: cooling at the top causes more condensation of ice, while cloud–base heating causes ice to evaporate. The result is that the cloud becomes less deep. At larger ice concentrations, the autoconversion term removes any ice that is formed by condensation due to infrared cooling. The main effect of the infrared radiation is to make the lapse rate less stable and thus cause more mixing of the ice.

Heckman (1991), Heckman and Cotton (1993), using the mesoscale version of RAMS for simulating cirrus clouds also concluded that in the absence of longwave radiative effects the atmosphere is more stable and less convective, clouds are thinner and there is less crystal generation. Suppressing the incoming shortwave radiation decreases the total cloud temperature, and a slight increase in stability is observed. When only vapor was allowed the effects clouds have on their environment can be emphasized: vertical motion is smooth and does not show cellular activity; the boundary layer is more realistic (is not as stable and reaches reasonable heights for midday); horizontal wind is smoother. It also shows that high supersaturations with respect to ice at high altitude were due to dynamically–forced moisture convergence. The only dissipation mechanism observed in these simulations appear to be evaporation due to subsidence. Areas of lower humidity were generally associated with weak downward motions but since the motions were weak, the drying did not occur instantaneously. As a result, clouds existed in areas of weak subsidence.

2.5 Conclusions

The cirrus models require a complete specification of the initial conditions, including the temperature and relative humidity profiles. In addition, environmental conditions which force the model - vertical motion and vertical shear of the horizontal wind - are important in the simulations. Errors in the assumed initial conditions significantly alter the simulation; due to the initial stable thermal structure no turbulence is generated. Sensitivity studies suggest that better agreement can be achieved if the vertical mixing is stronger. The number of ice crystals nucleated is strongly sensitive to the cooling rate and to the phase change activation energy (which is not known at cirrus temperatures).

Crystal shape choice may contribute to the discrepancies between the observed and modeled size distribution: the largest crystals are very irregular while in most models the result of coagulation of two cylinders is to be a larger cylinder. Coagulation would probably increase the complexity of particle shape, and the surface area–to–mass ratio should increase more rapidly with crystal size than assumed in the model. Also, the effect of shape on cloud radiative properties is difficult to evaluate because Mie scattering with equivalent volume or equivalent area spheres becomes increasingly inaccurate as the crystal aspect ratio increases, especially for scattering of solar radiation.

The potential importance of dynamical processes on scales too small to be resolved by a mesoscale model is another uncertainty as cirrus are frequently composed of small–scale generating regions which are associated with strong updrafts.

A better approach in simulating a clouds is the large–eddy simulation (LES) technique. It offers the advantage of being able to simulate explicitly the detailed cloud–scale circulations and properties of the cloud. One limitation is the fact that an LES model cannot resolve scales of motions larger than about 5 km and smaller than 50 m; that becomes more severe when the atmosphere is stably stratified or when the dominant scales of motion is less than 50 m. But compared with higher order closure models, the LES models are less sensitive to the details of turbulent closure parameterization. A two–dimensional LES is termed as a cloud–resolving model (CRM) and the equations for a two–dimensional model are of course not as accurate as for a LES model. CRM do not properly represent turbulent eddies (vortex stretching is not permitted in two dimensions); therefore, the scales of eddies are larger and entrainment processes are not well simulated. Two–dimensional models, due to the constraint in the energy cascade have the result of increasing circulation as the grid–mesh is refined. This grid–mesh–size sensitivity problem may be responsible for distorting certain physical processes. Nonetheless CRM are useful for examining the non–linear coupling between the explicitly represented microphysics, radiation, and the model dynamics. One–dimensional models, on the other hand are useful when testing a parameterization without the complexity of the full large–scale model. Because of this constraint, vertical motion can not be resolved explicitly and therefore rely mostly on predictive equations for turbulent kinetic energy. These closures are only crude approximations to the reality. One–dimensional models usually neglect some important terms involving covariances of perturbation quantities in the equations for the time evolution of the horizontally–averaged droplet spectrum leading to misrepresenting the cloud–drop activation. Also retarding the initial stages of precipitation growth in horizontally inhomogeneous layers. Neglecting the forcing terms and simply setting covariances between velocities and scalars in terms of a local scalar gradients and eddy–diffusivities may unrealistically project the forcing terms onto the resolved scales; it also may be a spurious source for the mean supersaturation profiles that are generated (*Stevens et al., 1997*).

Cirrus clouds are an important component of the planetary energy budget because of their large spatial extent and their strong interaction with both solar and infrared radiation fields. These clouds appear to be important for the development of precipitation in many mesoscale and large–scale atmospheric systems. Therefore, it is important to better understand the microphysical processes and their interaction with dynamical and thermodynamical fields.

Chapter 3

THE RAMS MODEL

3.1 Introduction

The numerical model used to simulate cirrus clouds is the RAMS model. RAMS stands for Regional Atmospheric Modeling System and it was developed at Colorado State University from a non–hydrostatic cloud model (*Tripoli and Cotton, 1982*) and a mesoscale model (*Mahrer and Pielke, 1977*) rewritten into a new code. It has a wide variety of parameters that makes it a powerful tool for simulating a large diversity of cloud systems with different physical characteristics.

RAMS prognoses the wind components (u,v,w), the ice–liquid water potential temperature (θ_{il}), perturbation Exner function ($\pi - \pi_0$), total liquid water mass mixing ratio, the mixing ratios and number concentrations of the various hydrometeor species. For the case studied, only the significant hydrometeors were allowed (rain, hail and graupel production was turned off). As diagnosed variables RAMS uses dry air density, temperature, potential temperature, and the mass mixing ratios of vapor and cloud water.

RAMS uses the standard Arakawa–C grid, staggered in both the vertical and horizontal directions. On such a grid, scalar variables are defined at the center of each grid volume, while the velocity components are defined on the faces of the grid volume.

The condition for the top boundary is to set w field to zero: "wall on top" condition. Since this condition induces reflection, a damping method for absorbing this wave energy is used, on which the model variables were nudged to a reference state, using the Rayleigh friction as a damping mechanism (*Clark, 1977*) or using a more recent approach suggested by *Dr. Cotton* and described in *Cram (1990)* which involves nudging to a horizontal running average ($\bar{X}$):

$$\left(\frac{\partial X}{\partial t}\right)_{nudge} = \frac{X - \bar{X}}{\tau}. \tag{3.1}$$

For this simulation this technique is applied for velocity fields, perturbation Exner function, ice–liquid water potential temperature, pristine ice and total mixing ratios. The horizontal running average variables ($\bar{X}$s) are taken from a previous run of RAMS setup as a CRM model, and then interpolated at the new grid levels. For the parameter τ a value of 600 s was chosen.

The code was also modified to include the effects of vertical diffusion of velocity as described in *Kosovic (1996)*. Details about this code can be found in *Wu (1998)*. For the lateral boundary, RAMS was set on with cyclic boundary conditions and for the bottom boundary, beside setting w to zero, a constant surface temperature is assumed (i.e. the temperature of the sea (SST)).

RAMS has the capability of using either cartesian coordinates or polar–stereographic as a horizontal grid. The vertical coordinate is σ_z terrain following system (*Clark and Farley, 1984*). The vertical grid spacing can be also specified by the user which makes it very useful when the purpose is to simulate the physical processes in some detail at some height in the atmosphere. In this thesis the sought for detailed structure is at the height of tropical cirrus clouds (around 9 km).

3.2 RAMS microphysics

In general, in RAMS (*Walko et al., 1995, Meyers et al., 1997*) water is divided into eight categories: vapor, cloud droplets, rain, pristine ice, snow, aggregates, graupel and hail. Cloud droplets and rain are liquid water, but may be supercooled. Pristine ice, snow and aggregates are assumed to be solid, while graupel and hail are treated as mixed–phase categories, thus they can consist of ice only or a mixture of ice and liquid.

Cloud droplets and pristine ice can only nucleate from vapor. All other categories form from existing hydrometeors, and after that can grow by vapor deposition. Pristine ice consists of relatively small ice crystals, while larger ones are considered to be snow (*Harrington et al., 1995*). Pristine ice once formed may continue to grow through vapor deposition while ice crystals in the snow category are supposed to have grown by vapor deposition as well as riming. These two categories enables a bi–modal representation for ice crystals.

Aggregates are those ice crystals that have formed as a result of collision and coalescence of pristine ice, snow, and/or other aggregates.

Hydrometeors in each category are assumed to be distributed according to a generalized gamma distribution described by *Flatau et al. (1989)* and *Verlinde et al. (1990)*:

$$f_{gam}(D) = \frac{1}{\Gamma(\nu)}\left(\frac{D}{D_n}\right)^{\nu-1}\frac{1}{D_n}exp\left(-\frac{D}{D_n}\right). \tag{3.2}$$

The shape parameter $\nu \geq 1$ controls the relative amount of smaller vs. larger hydrometeors in the distribution. The characteristic diameter D_n is used to nondimensionalize D ($D_{mean} = \nu D_n$).

This formulation is useful when computing any moment P of the distribution:

$$\int_o^\infty D^P f_{gam}(D)dD = D_n^P\frac{\Gamma(\nu+P)}{\Gamma(\nu)} \tag{3.3}$$

since mass ($m = \alpha_m D^{\beta_m}$), mass mixing ratio ($r = \frac{N_t}{\rho_a}\alpha_m D_n^{\beta_m}\frac{\Gamma(\nu+\beta_m)}{\Gamma(\nu)}$) and terminal velocities ($v_t = \alpha_{vt}D^{\beta_{vt}}$) can be expressed as powers of D. Fall velocity is considered to be a function of diameter and category.

For each hydrometeor category five parameters ($\nu, \alpha_m, \beta_m, \alpha_{vt}, \beta_{vt}$) can be selected. For pristine ice and snow, sets of these parameters can be switched in order to simulate different crystal habits.

With the exception of cloud water and vapor, all the hydrometeors plus an additional "total water" category varies according to the following expression:

$$\frac{\partial r}{\partial t} = ADV(r) + TURB(r) + SOURCE(r) + SEDIM(r) \tag{3.4}$$

where r stands for the mixing ratios of rain, pristine ice, snow, aggregates, graupel, hail and total water categories. $ADV(r)$ and $TURB(r)$ represent advective and turbulent transport of r by the resolved and subgrid velocities. $SOURCE(r)$ represents the source/sink terms which consist of all types of conversion between categories. $SEDIM(r)$ counts for local losses/gains of mixing ratio due to gravitational sedimentation. The above equation is integrated forward in time to prognose mixing ratios.

As mentioned before, having r determined either prognostically or diagnostically, one more distribution parameter (N_t or D_n) must be determined so that the other one may be diagnosed. RAMS has the options to choose between: (1) specify N_t, (2) specify D_n, (3) prognose N_t (not for cloud water), (4) specify N_0 (for the case when $\nu = 1$; $N_t = N_0 D_n$). Note that N_t is always prognosed for pristine ice since this is the category into which nucleated ice is introduced. For all the other species one of the above options can be used.

According to *Verlinde et al. (1990)*, the rate at which the mixing ratio r_x of species x is collected into coalesced hydrometeors due to collisions with hydrometeors of species y is given by the stochastic collection equation:

$$\frac{dr_x}{dt} = \frac{N_{tx} N_{ty} \pi F_\rho}{4\rho_a} \int_0^\infty \int_0^\infty m(D_x)(D_x + D_y)^2$$

$$\mid v_{tx}(D_x) - v_{ty}(D_y) \mid f_{gamx}(D_x) f_{gamy}(D_y) E(x,y) dD_x dD_y \tag{3.5}$$

where $F_\rho = \rho_a^{-0.5}$ accounts for density effect on the terminal fall velocities. The collection efficiency $E(x, y)$ is the product of collision efficiency and coalescence efficiency and assuming it is independent of D_x and D_y for all hydrometeors classes but cloud droplets, analytic solutions can be found for the above equation. In the more recent code of RAMS, full 3D lookup tables are used to speed up computational time. Two of the table dimensions are the characteristics diameters D_x and D_y - divided into 60 uniform logarithmic intervals, while the third dimension is the pair (x,y) of interacting category. From the total of 49 possible interactions, only 32 are considered to be possible. These are divided into two classes, each with its own basic rules for determining the destination category or categories to which the mixing ratio Δr_x is transferred. One class treats collisions between liquid and liquid or between ice and ice. In this class, destination category is a single category, determined only by the interacting hydrometeors. Table 3.1 lists these possible interactions. The other class treats mixed–phase interactions: cloud water or rain with any of the ice category (except that between cloud water and pristine ice which is neglected). For this class, two collection amounts are computed: one for liquid collected by ice and one for ice collected by liquid. Depending on the energy of the resulted hydrometeor, then the total mixing ratio is either transferred to liquid or is divided between the input ice category and a secondary ice category. This secondary ice category is graupel in the case of cloud water and hail for rain. As mentioned earlier, in the case of collision and coalescence of cloud droplets, due to the strong variations of $E(x, y)$ and due to the large gap in diameters of cloud droplets and rain, a separate autoconversion parameterization proposed by *Berry and Reinhardt (1974)* is used. The latest version of RAMS uses a new autoconversion scheme developed by *Feingold et al. (1997)* in which E is not assumed to be unity. This was not used in this study, however.

For describing the nucleation of pristine ice two physical mechanisms are used: homogeneous nucleation and heterogeneous nucleation.

Homogeneous nucleation of supercooled water is a spontaneous process in which a crystal lattice structure is formed in a water droplet due to random motion. After this structure is formed, it quickly grows throughout the drop. According to *DeMott et al. (1994)*, the number of cloud droplets freezing in a timestep is:

$$(N_t)_c = N_t \int_0^\infty [1 - e^{-10^{\Phi(T)} \frac{\pi D^3}{6} \Delta t} n(D)] dD \tag{3.6}$$

Table 3.1: Collected, Collecting and Destination Category. From *Walko et al. (1995)*

Collected category	Collecting category	Destination category
cloud water	rain	rain
pristine ice	pristine ice	aggregates
pristine ice	snow	aggregates
snow	pristine ice	aggregates
pristine ice	aggregates	aggregates
pristine ice	graupel	graupel
pristine ice	hail	hail
snow	snow	aggregates
snow	aggregates	aggregates
snow	graupel	graupel
snow	hail	hail
aggregates	graupel	graupel
aggregates	hail	hail
graupel	hail	hail

where $\Phi(T) = -606.3952 - 52.6611\,T - 1.7439\,T^2 - 0.0265\,T^3 - 0.0001536\,T^4$ (*Eadie, 1971*). The above integral (3.6) can also be pre–computed for the temperature range [-50°C, -30°C], while for temperatures below -50°C the value at -50°C is assumed to be a valid approximation. In such a way, a two–dimensional lookup table is created.

The fraction of haze particles freezing in a Δt time step is:

$$(N_t)_h = N_h[1 - e^{-f_{nuc}\Delta t}] \tag{3.7}$$

where N_h is the number concentration of haze particles and the fractional number of haze particles freezing homogeneously in a unit time is given by (*DeMott et al., 1994*):

$$f_{nuc} = \int_0^{D_{max}} \left(\frac{D}{D_n}\right)\left[1 - exp\left(\frac{D}{D_e}\right)^b\right]\frac{dD}{D_n}.$$

Here D and D_n describes the CCN spectrum - assumed to follow a gamma distribution - and D_e and b are functions of temperature and relative humidity. As before, this integral can also be pre–calculated and stored in a two–dimensional lookup table.

In the case of heterogeneous nucleation, the initial ice crystal formation is on an ice nucleus (IN).

Deposition nucleation and condensation–freezing are both forms of heterogeneous nucleation. In the first case, vapor molecules attach to an IN, while in the second case vapor molecules form as liquid on the aerosol owing to its hydroscopic property, then freeze due to its IN property. These two processes are represented by an empirical formula described by *Meyers et al. (1992)*:

$$(N_t)_d = exp(6.269 + 12.96 r_{si}) \tag{3.8}$$

where r_{si} is the supersaturation with respect to ice.

Another heterogeneous process that may occur is contact freezing nucleation, and occurs when an IN comes into contact with an existing supercooled cloud water droplet. The IN is transported near the supercooled cloud water droplet by a combination of diffusiophoresis, thermophoresis and Brownian motion as described in *Cotton et al. (1986)*. The numbers of ice crystals produced in a time step by contact freezing nucleation in this case is proportional to the cloud droplet concentration (N_{tc}) and the concentration of active contact nuclei (N_a). Based on laboratory experiments, *Meyers et al. (1992)* estimated the number of IN available for contact freezing nucleation as:

$$N_a = exp(4.11 - 0.262T). \tag{3.9}$$

Adding up all these processes the total number of nucleating ice crystals (pristine ice) is given by the sum:

$$\Delta N_t = (N_t)_d + (N_t)_c + (N_t)_h + \left[\left(\frac{dN_t}{dt} \right)_v + \left(\frac{dN_t}{dt} \right)_t + \left(\frac{dN_t}{dt} \right)_b \right] \Delta t \tag{3.10}$$

where the last three terms represent the contribution to the number of ice crystals produced by contact nucleation due to diffusiophoresis, thermophoresis and Brownian motion respectively. Following this, the contribution to mixing ratio is then:

$$\Delta r_p = \Delta N_t m_n / \rho_a \tag{3.11}$$

where m_n is an assumed initial mass of a nucleated particle and ρ_a is the dry air density.

As mentioned before, for pristine ice the number concentration is prognosed using an equation in the same form as equation (3.4). Since in this particular situation the mixing ratio and concentration may be inconsistent with each other, a check on the characteristic diameter is made in order to make sure that the value is within some predefined limits. If the diagnosed diameter is out of bounds then the concentration is re–diagnosed based on that limiting diameter.

Beside these processes, other processes can contribute to ice production.

One of these is the secondary ice production based on Hallett–Mossop theory which is parameterized according to *Cotton et al. (1986)*:

$$P_p(I) = 3.5 \times 10^5 g^{-1} \left(\frac{dm}{dt}\right)_{riming} \times \begin{cases} 0 & ,T > 270.16 \\ (T - 268.16)/2. & ,T\epsilon(270.16, 268.16) \\ (T - 268.16)/3. & ,T\epsilon(268.16, 265.16) \\ 0 & ,T < 265.16 \end{cases} \tag{3.12}$$

where T is the surface temperature of the ice particle and $\left(\frac{dm}{dt}\right)_{riming}$ is the riming rate.

When pristine ice grows by vapor deposition a transfer from this category to snow is performed. If the snow evaporates the reverse process applies. This is made in order to make the distinction between pristine ice and snow: a constant threshold diameter $D_b = 125$ μm based on measurement in cirrus clouds is used (*Harrington, 1994*).

RAMS uses a Lagrangian scheme for sedimenting the mixing ratio from any grid point to a lower height (*Walko et al., 1995*). This is performed by identifying the mixing ratio as a collection of volumes each corresponding to a grid cell that is bounded by a top and a bottom height. Since sedimentation deals only with the mass–weighted relative fall velocities between the hydrometeor and air, the key in solving (3.4) is to first solve it without the $SEDIM$ term; then the updated r is applied only to $SEDIM$ term. In this case the new top and bottom of the grid cell is computed by a simple translation with the value of $V_t \Delta t$ and redistribute the mixing ratio r to the cells on which the transported initial grid cell overlaps. In such a way, it is possible to have sedimentation that is more rapid than one grid level per timestep. In evaluating the $SEDIM$ term for number concentration for each hydrometeor, it is assumed that N_t is transported in the same proportion as mixing ratio.

3.3 RAMS radiation scheme

Because radiation is an important contribution to a cirrus cloud life cycle, a new radiation code was used. This new code provides an alternative to the other two options RAMS offers. The first, developed by *Mahrer and Pielke (1977)* includes the effects of water vapor, CO_2 and O_3 but ignores the effects of clouds. The second is one developed by *Chen and Cotton (1983)* and includes the effects of condensate, but as it uses the total mixing ratio to calculate the radiative transfer it does not differentiate between liquid water and ice, nor the size distribution of the hydrometeors. The third option was developed by *Harrington (1997)* and is described below.

For this simulation, option three was used. This broad band two–stream model, described in *Harrington (1997)*, is limited to three solar bands and five infrared bands. In a two–stream model, the radiative transfer equation is averaged so that the upwelling and downwelling fluxes are obtained. These two fluxes are of a major importance in a numerical model because the radiative heating/cooling rates are proportional to the net flux divergence within a grid volume.

The interaction of the two–stream model with the cloud, requires the definition of three fundamental parameters: optical depth, single scatter albedo and asymmetry parameter. In the past models, the assumption of "grey" (independent of wavelength) optical properties was common. But for the near infrared portion of the solar spectrum, as the complex index of refraction of liquid water and ice varies over several orders of magnitude, this assumption is poor. The cloud optical properties was performed using the solar and infrared energy per wavelength method developed by

Slingo and Schrecker (1982). In order to adjust for the over–absorption, the complex index of refraction was artificially limited to its mean value in the near infrared band. A modified version of Anomalous Diffraction Theory (ADT) as described in *Mitchell (1997)* that accounts for internal reflection/refraction, resonance tunneling and edge effects for the liquid–phase microphysics is implemented. For the ice–phase the work of *Mitchell and Arnott (1994)*, *Mitchell et al. (1996)* and *Auer and Veal (1970)* is used.

For computing the radiative effects, since the model top level is at 13500 m, in order to ensure correct calculations for radiative effects, a standard profile for pressure, temperature, density, vapor mixing ratio and ozone density is added at each grid point. But this standard profile will give us the same profile above the top model for each grid point, hence the possibility of strong gradients for temperature, vapor mixing ratio and density, not to mention the possibility of having totally different values for heights - as we use pressure as the interpolation variable. In order to avoid that, for all these variables we assume continuity at the model top and define shifted values defined by:

$$\Delta X = X_{top} - X_{profile} \tag{3.13}$$

where X_{top} is the value at the model top and $X_{profile}$ is the value interpolated from the standard profile at the same pressure. Then, as new levels are added each variable is assumed to have a new value given by:

$$X_{new}(z) = X_{profile}(z) + \Delta X \times exp(-\frac{z - z_{top}}{\Delta z}) \tag{3.14}$$

where $X_{profile}(z)$ is the value interpolated from the standard profile, z is the level added and $\Delta z = 3000$ m. The new level z is computed using the hydrostatic approximation and the equation of state. In such a way we can ensure the continuity for our variables and as we add more levels we approach the standard profile.

3.4 Model Initialization

As mentioned before, as input data for this simulation, data from a previous RAMS–CRM run was used. The run started with the date of December 20^{th} 1992, and ended six days latter, in an attempt to simulate cirrus cloud evolution over the central region of TOGA COARE. For that run, RAMS was run with a horizontal grid space of 1000 m, a variable vertical grid spacing (500 m at clouds level) and the time step set to 10 s. The initial field variables were assumed to be homogeneous and a perturbation noise with 0.5 K amplitude was uses to "disturb" the temperature field. As it will be explained in the next chapter, these simulations are part of the GCSS Working Group # 4 strategy for developing and improving parameterizations of cloud systems that can be used in climate and numerical weather prediction models.

The case to study was chosen to be on December 22^{nd} 1992. The simulations started at 06:00 GMT and lasted till 24:00 GMT.

Two cirrus cloud simulations over the same period of time and space were performed: one as a two–dimensional model and one as a three–dimensional model. The grid configuration (only one grid is used) was 50x1x114 for the 2D simulation and respectively 50x50x114 for the 3D simulation. The projection used is cartesian, centered at 2°S and 156°E (same as in the RAMS–CRM, and the center of the TOGA COARE). The horizontal grid spacing is set to 100 m, while vertical grid spacing is variable, but set to 50 m at clouds level. It uses 114 vertical grid points with a top at 13500 m (see Table 3.2 for the vertical setting).

The time step is set to 1 s and a hybrid numerical scheme is used for time integration.

The initial sounding was "constructed" from the RAMS–CRM run, interpolated at the levels of interest (see Figure 3.1).

When initializating RAMS, beside the data used as input in a sounding format, the vertical velocity was initialized too. An initial perturbation with a 0.5 K amplitude

Table 3.2: Vertical levels used in the runs (in m)

0.0	100.0	250.0	500.0	1000.0	1500.0	2000.0	2500.0
3000.0	3500.0	4000.0	4500.0	5000.0	5500.0	5750.0	6000.0
6250.0	6500.0	6750.0	6800.0	6850.0	6900.0	6950.0	7000.0
7050.0	7100.0	7150.0	7200.0	7250.0	7300.0	7350.0	7400.0
7450.0	7500.0	7550.0	7600.0	7650.0	7700.0	7750.0	7800.0
7850.0	7900.0	7950.0	8000.0	8050.0	8100.0	8150.0	8200.0
8250.0	8300.0	8350.0	8400.0	8450.0	8500.0	8550.0	8600.0
8650.0	8700.0	8750.0	8800.0	8850.0	8900.0	8950.0	9000.0
9050.0	9100.0	9150.0	9200.0	9250.0	9300.0	9350.0	9400.0
9450.0	9500.0	9550.0	9600.0	9650.0	9700.0	9750.0	9800.0
9850.0	9900.0	9950.0	10000.0	10050.0	10100.0	10150.0	10200.0
10250.0	10300.0	10350.0	10400.0	10450.0	10500.0	10550.0	10600.0
10650.0	10700.0	10750.0	10800.0	10850.0	10900.0	10950.0	11100.0
11150.0	11200.0	11300.0	11400.0	11600.0	11800.0	12000.0	12500.0
13000.0	13500.0						

was applied to the temperature field. For the nudging procedure (made at every time step) files containing velocity field, perturbation Exner function, ice–liquid water potential temperature, pristine ice and total mixing ratios obtained from the CRM run at every 15 minutes are used. In Figure 3.3 are presented the time evolution for pristine ice and aggregates mixing ratios and, as one can see from the pristine ice mixing ratio time evolution, a two layer cirrus cloud separated by a region with a relatively strong gradient was present.

Radiation effects were computed at every other grid point and updated at every 15 minutes. In the microphysics module, rain, graupel and hail production was turned off as for high altitude tropical cirrus these hydrometeors are unlikely to be present. The coefficient ν in the gamma distribution was set to two for all hydrometeors. The runs produced a cirrus cloud with its base around 8000 m and top around 11200 m (for both two–dimensional and three–dimensional runs). A discussion about the differences and the characteristics of each run is made in chapter five.

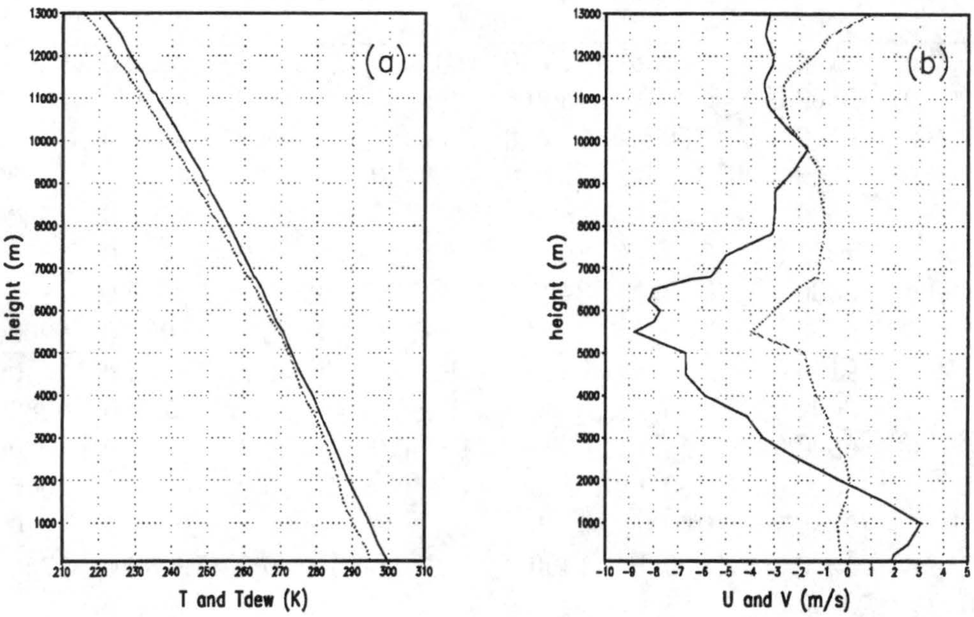

Figure 3.1: (a) initial profiles of Temperature (solid line) and dew–point Temperature (dash line); (b) initial profiles of U (solid line) and V (dash line)

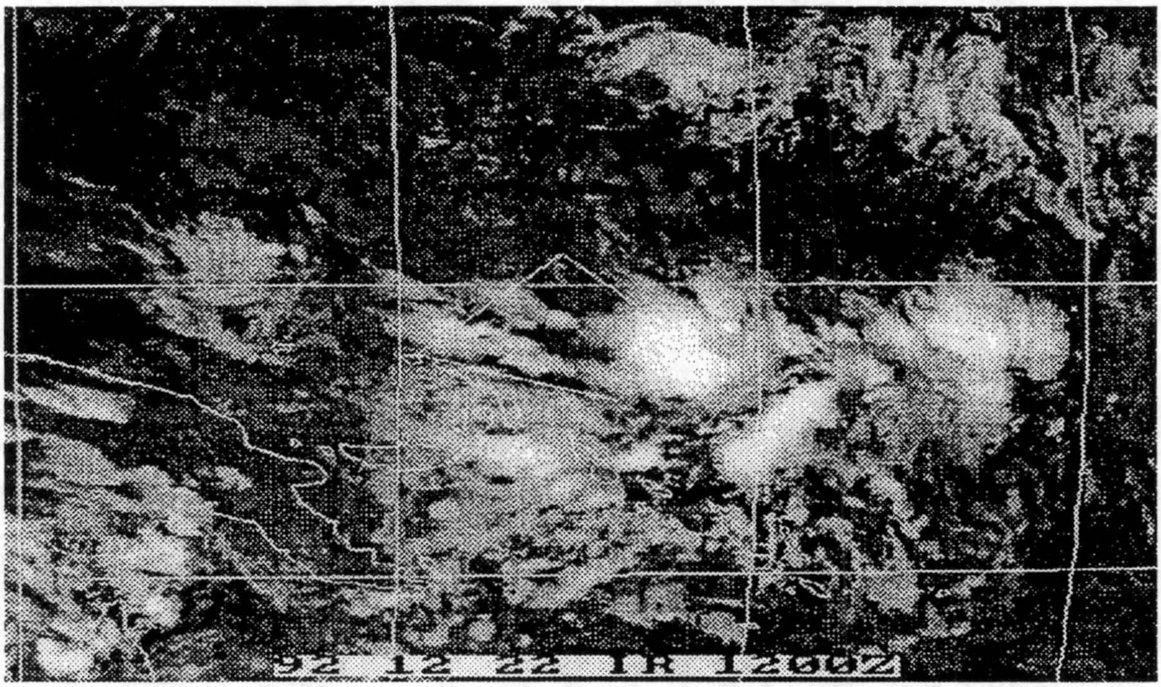

Figure 3.2: IR satellite image for the 22^{nd} December 1992 12:00 GMT

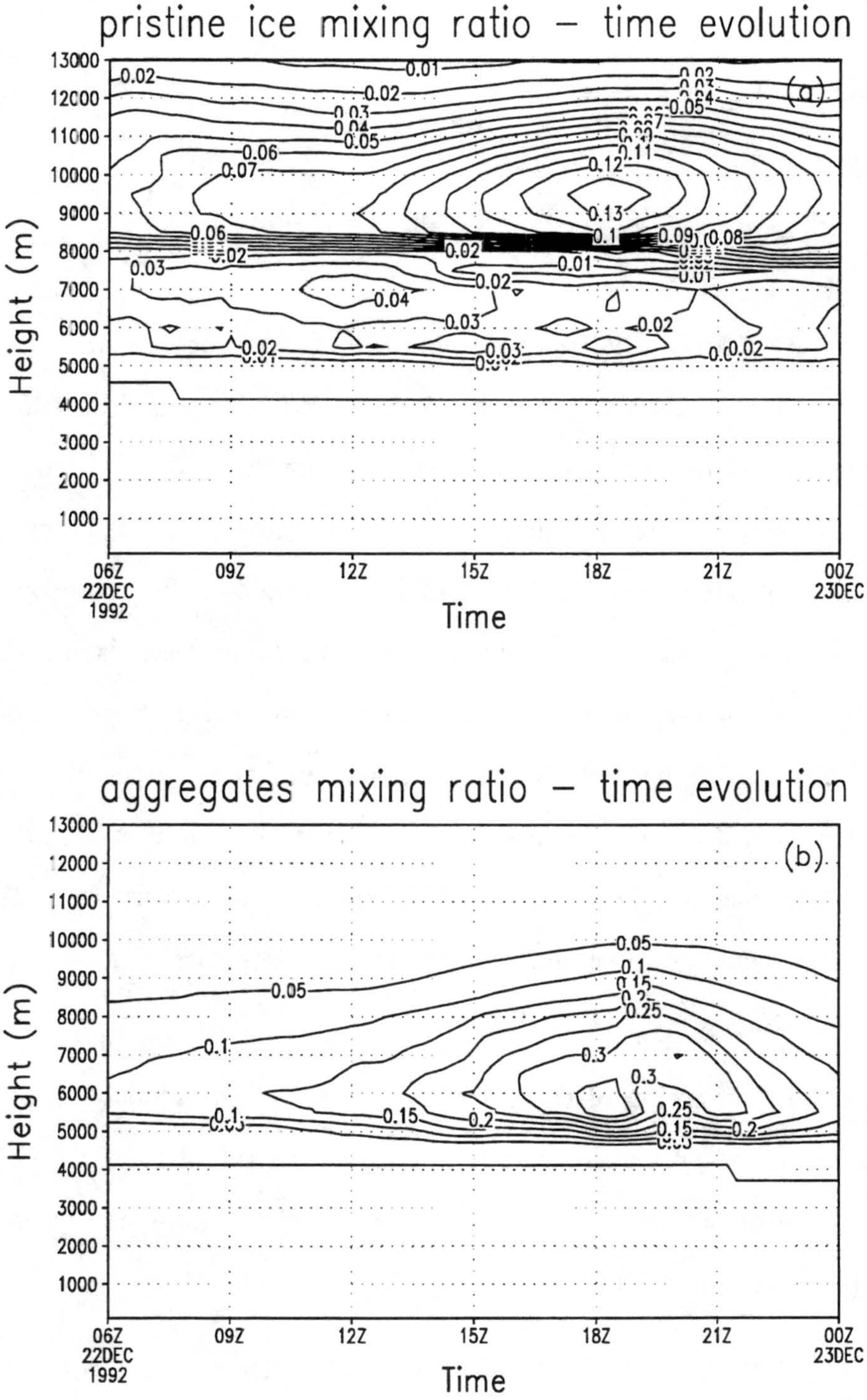

Figure 3.3: RAMS–CRM simulation. (a) pristine ice mixing ratio time evolution; (b) aggregates mixing ratio time evolution.

Chapter 4

TOGA COARE

The Tropical Ocean Global Atmosphere (TOGA) program was a major component of the World Climate Research Program (WCRP) aimed specifically at the prediction of climate phenomena on time scales of months to years. It emphasizes the tropical oceans and their relationship to the global atmosphere, based on the premise that the dynamic adjustment of the ocean in the tropics is far more rapid than at higher latitudes. Thus disturbances emanating from the western Pacific Ocean (such as *El Niño*) may propagate across the basin on time scales of weeks compared to years for corresponding basin–wide propagation at higher latitudes. The significance of shorter dynamic times scales near the equator is that they are similar to those of highly energetic atmospheric modes. This similarity allows the formation of coupled modes between the ocean and the atmosphere. The specific goals and scientific objectives of TOGA are (WCRP, 1985):

- To gain a description of the tropical oceans and the global atmosphere as a time dependent system in order to determine the extent to which the system is predictable on time scales of months to years and to understand the mechanisms and processes underlying its predictability.

- To study the feasibility of modeling the coupled ocean-atmosphere system for the purpose of predicting its variation on time scales of months to years.

- To provide the scientific background for designing an observing and data transmission system for operational predication, if this capability is demonstrated, by coupled ocean–atmosphere models.

A series of national, multinational and international efforts (e.g., NAS, 1986; WCRP, 1986) made it possible to achieve the TOGA goals. It was during this program that it has been demonstrated the relative importance of the Atlantic, Indian and Pacific ocean basins in producing the interannual *El Niño–Southern Oscillation* (ENSO) signal, with the Pacific ocean the main factor (*Webster and Lukas, 1992*). Following ENSO variations in the Pacific structure, the Atlantic and Indian oceans are affected by the anomalous wind forcing originating in the Pacific. But some concerns emerged: unexplained estimates of the order of 60–80 W/m^2 in the surface energy balance (*Godfrey and Lidstrom, 1988*); too warm oceans when models use heat fluxes derived from climatological data or derived from atmospheric models; weaker modeled westerly winds in the western Pacific than observed in nature (*Hirst, 1988, Cane, 1990*). All these model failures showed the need for more measurements in the warm–pool regions of the Pacific Oceans.

TOGA Coupled Ocean–Atmosphere Response Experiment (COARE) was designed to address the concerns listed above and has the basic task of obtaining a dataset that allows the study of the local and remote modes of communication between the atmosphere and the ocean. The scientific goals of TOGA COARE are to describe and understand (*Webster and Lukas, 1992*):

- The principal processes responsible for the coupling of the ocean and the atmosphere in the western Pacific warm pool system;
- The principal atmospheric processes that organize convection in the warm pool region;
- The oceanic response to combined buoyancy and wind stress forcing in the western Pacific warm pool region;
- The multiple scale interactions that extend the oceanic and atmospheric influence of the western Pacific warm pool system to other regions and vice versa.

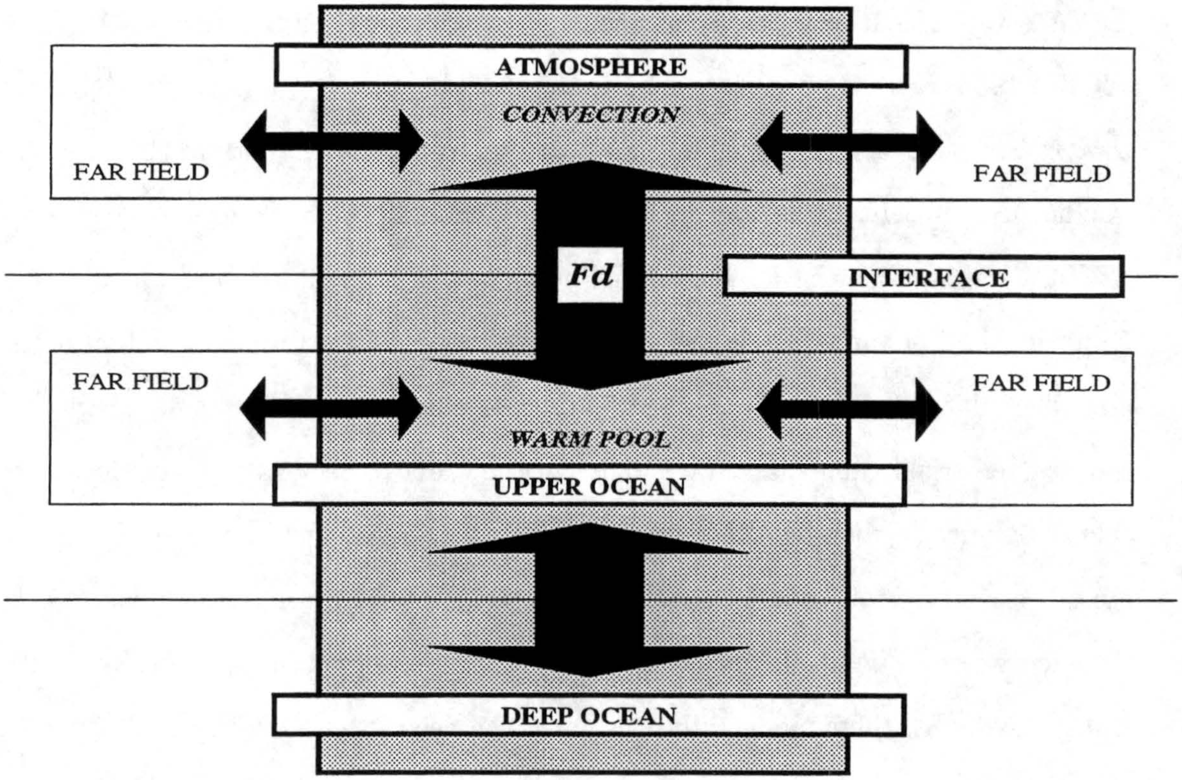

Figure 4.1: Schematic representation of the experimental design of the IOP of COARE.

The goals of TOGA COARE are designed to provide an understanding of the role of the warm pool regions of the tropics in the mean and transient state of the tropical ocean–atmosphere system. These goals will lead to improved parameterizations of heat and fresh water fluxes between ocean and atmosphere, required for better performance of short and long–term oceanic and coupled atmospheric and oceanic climate prediction models.

Figure 4.1 shows a schematic representation of the TOGA COARE experimental design. The vertical box represents the zone of maximum concentration of effort and resources. This innermost domain is referred to as the intensive flux array (IFA). Its main goal is to determine the interfacial fluxes (noted Fd) within a relatively small area of the warm pool. Meanwhile, the response of the ocean is monitored within the vicinity of the observed atmospheric forcing and determine the transmission of the signals to and from the larger–scale, or far–field, atmosphere and ocean.

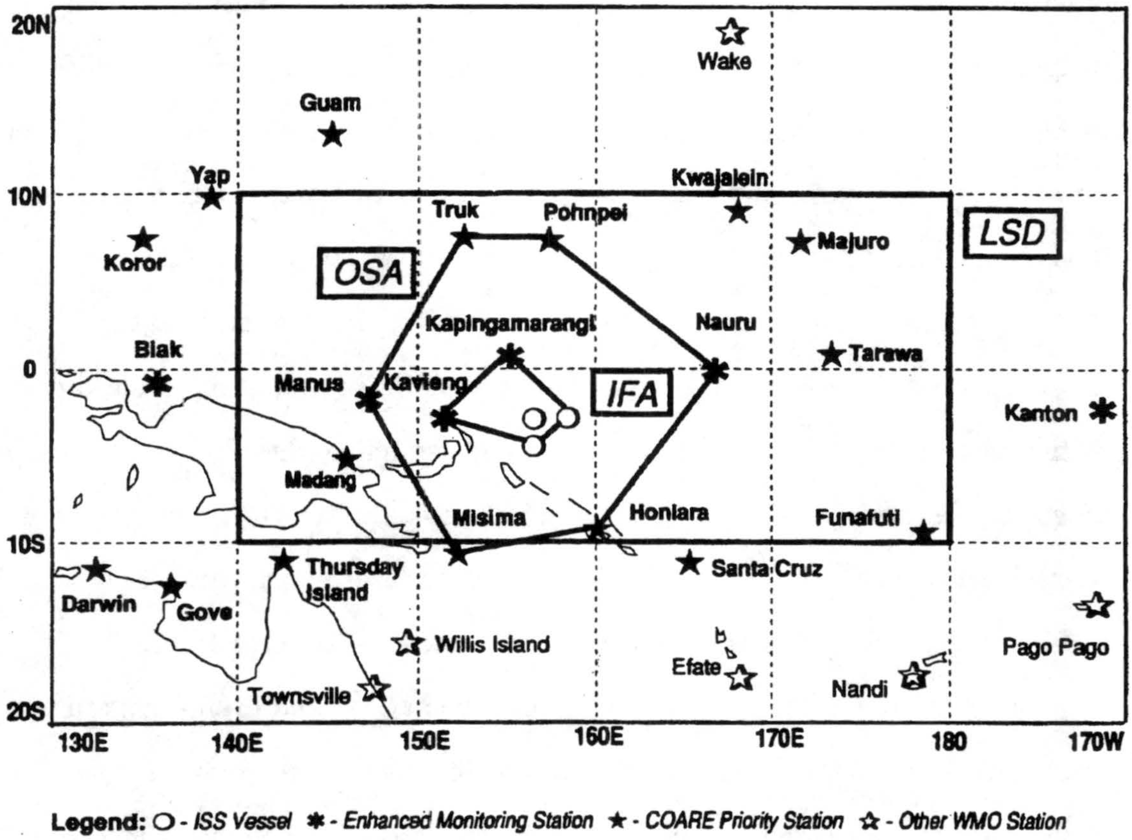

Figure 4.2: Composite structure of the intensive observation period of TOGA COARE: (LSD): the large–scale domain; (OSA): the outer sounding array; (IFA): the intensive flux array. From *Webster and Lukas (1992)*

On Figure 4.2, the three characteristic TOGA COARE domains can be seen:

- Large–Scale Domain (LSD): contains the warmest waters, is the most convectively disturbed and receives the greatest amount of precipitation in the tropical Pacific Ocean;
- Outer Sounding Array (OSA): defined by the meteorological stations at Truk, Ponape, Nauru, Honiara and Kavieng.
- Intensive Flux Array (IFA): centered at 2°S and 156°E

The atmospheric measurements lasted one year starting July 1992, while the oceanic monitoring started September 1992 and ended October 1993. The intense observation period (IOP) lasted from November 1992 to February 1993. The observations consisted of a multitude of in situ measurements and remote satellite observations, then used to characterize and quantify the processes of interaction between atmosphere and ocean, and also the relationship of the warm–pool features to the larger–scale structures.

This complete and complex dataset is very useful for the initialization and validation of coupled models and to further understanding of short time–scale variability of the heat, moisture, momentum fluxes, understanding the physics of interfacial processes, determining the synoptic and mesoscale structure in the warm–pool; determining the space–time variability of the sea surface temperature (SST) and sea surface salinity (SSS) and the processes that influence these structures.

The next step is that of performing intercomparison and evaluation studies between several CRMs, using these observations in order *"to develop better parameterization of cloud systems for climate and numerical weather prediction models via an improved understanding of coupled physical processes"*. In fact this is the main objective of the GEWEX (Global Energy and Water–Cycle Experiment) Cloud System Study (GCSS) Working Group # 4 (Precipitating Convective Cloud Systems working group) (*Moncrieff et al. 1996*). In order to make a proper evaluation of each model performance, all models need to be set in the same way: same vertical and horizontal structure and same field profiles as initialization (large–scale temperature, mixing ratio and velocity components; SST, surface pressure and profiles of the large–scale advective tendencies of temperature and mixing ratio).

The simulations span over a six day period (20^{th} December - 25^{th} December 1992), during a westerly wind burst that has much relevance to ocean–atmosphere interaction. The objectives of these simulations are to improve knowledge of the large–scale effects of convective processes and its parameterization in numerical weather prediction models and general circulation models.

Chapter 5

CASE STUDY: 22 DECEMBER 1992

5.1 Introduction

This chapter is dedicated to an analysis of a cirrus cloud that forms during a simulation over a region centered at 2°S and 156°E over the Western Pacific. As explained in chapter three, two cirrus cloud simulations were performed: one using RAMS in a two–dimensional configuration, and the other one in the three–dimensional configuration. An 18 hour run, starting at 06:00 GMT 22^{nd} December 1992, for both configurations was performed. The purpose of these runs is to see how well RAMS, configured as an LES model, describes the physical parameters that are characteristic to a tropical cirrus cloud and to further our understanding of tropical vs. extra–tropical cirrus clouds.

Since one of the objectives of TOGA COARE is to determine new parameterizations that can be used in single–column models, the probability distribution function for vertical velocity is computed and it is shown that is well approximated by a gaussian distribution. This will prove useful when computing various terms that depend on vertical velocity in the microphysical module of a single column model.

5.2 3D run

For the three–dimensional case, a thick cirrus cloud forms a few moments after initialization. It has a base at approximately 8000 m and the top is at 11200 m and as one can see from Figure 5.1 (a), it was almost steady state.

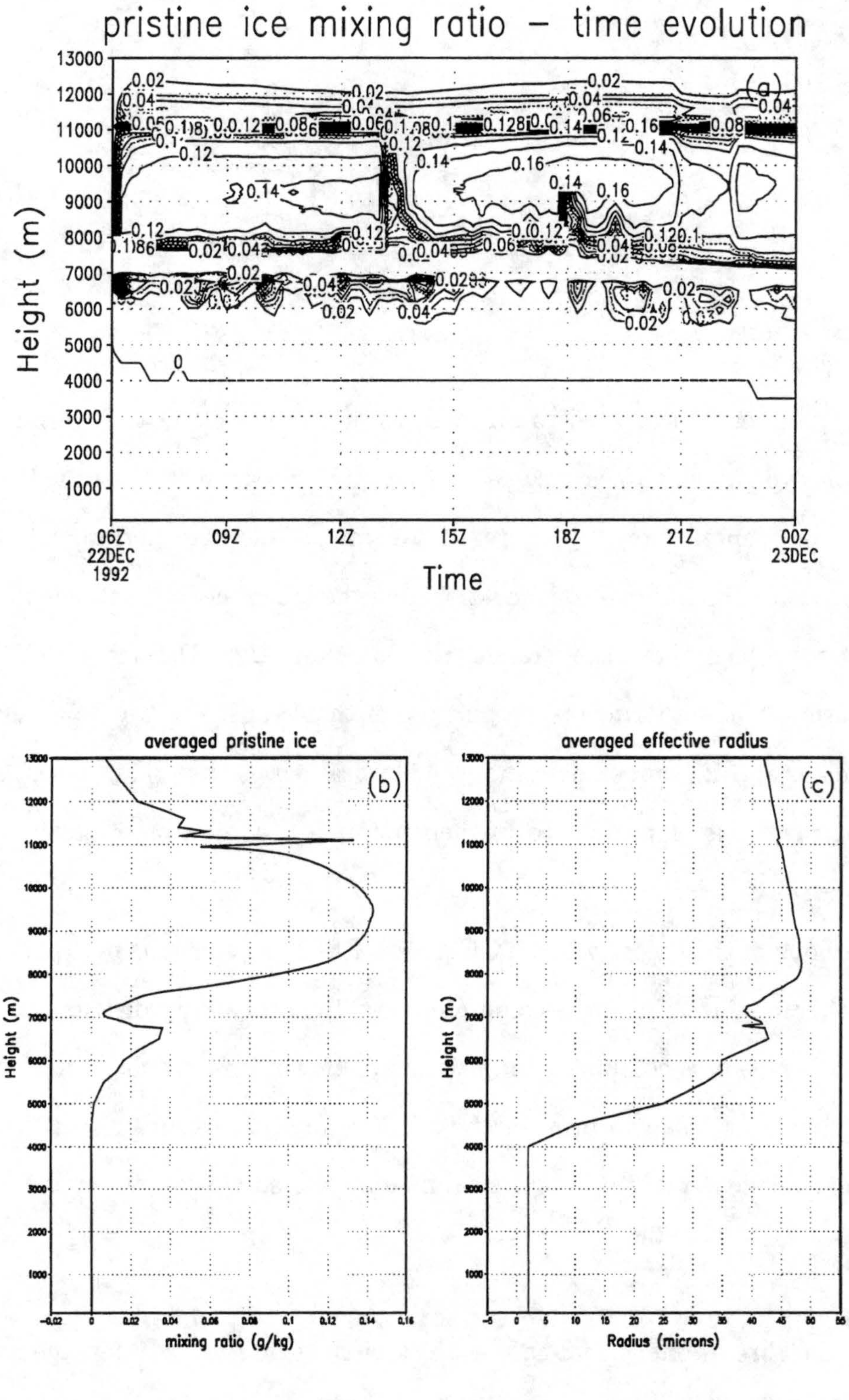

Figure 5.1: 3D simulation. (a) pristine ice mixing ratio time evolution; (b) averaged pristine ice mixing ratio distribution; (c) averaged pristine ice effective radius distribution.

The pristine ice mixing ratio is about 0.14 g/kg. The averaged[1] pristine ice mixing ratio (Figure 5.1 (b)) shows three maxima. The main one is within the cloud at about 9500 m. The one that appears below the cloud at about 6700 m is associated with processes that involves phase transformation, while the one that appears at the top of the cloud is associated with intense radiative cooling. The maximum mean effective radius is about 48 microns and decreases with height as expected (Figure 5.1 (c)). This is comparable with measurements made by *Heymsfield and McFarquhar (1996)*, when a mean radius of 30 microns was found during the Central Equatorial Pacific Experiment (CEPEX).

Figure 5.2 shows the time evolution for snow mixing ratio (a), and aggregates mixing ratio respectively (b). These figures illustrate a two–layer cloud separated by a relatively dry layer: one between 5000 - 7000 m composed mainly of aggregates and snow, and the main one, composed of pristine ice, aggregates and snow from 8000 to 11200 m. The existence of this dry layer can also be argued from the region of strong gradient that is present for both pristine ice and snow mixing ratio distribution that RAMS–CRM run produced (see Figure 3.3 (a)). The fact that in that run, the dry layer is not very well resolved may be due to the poor vertical resolution used (500 m, while the dry layer is 1000 m thick). Figure 5.2 also displays the fact that the bottom of the main cloud layer decreases with time, and so does the top and bottom of the secondary layer and this is probably associated with a slight decrease in temperature at these levels over time. The top of the main layer remains practically at the same altitude. When adding the contribution of all three hydrometeors, the ice content varies from approximately 0.5 g/kg at cloud base (at 8000 m) to 0.01 g/kg at the top of the cloud (11200 m). This is consistent with measurements made by *McFarquhar and Heymsfield (1996a)* for tropical anvils during CEPEX, where the values ranged from less than 0.01 g/kg at cloud top and reached 1.0 g/kg at cloud base. For the

[1]the averaged period of time: 06:00 GMT to 24:00 GMT unless otherwise specified

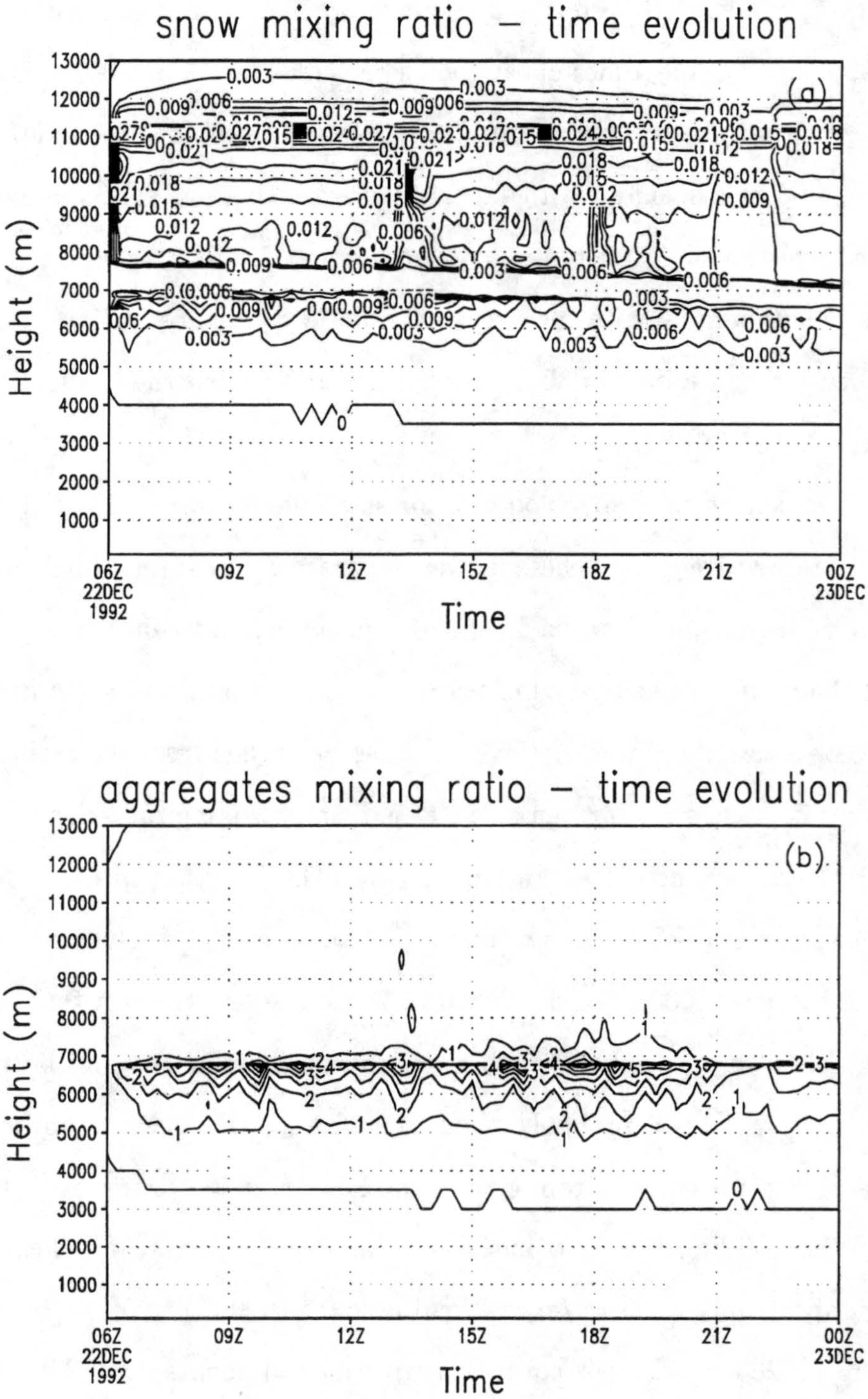

Figure 5.2: 3D simulation. (a) snow mixing ratio time evolution; (b) aggregates mixing ratio time evolution.

second cloud layer, the ice content is given by the aggregates mixing ratio and it ranges from 1 g/kg to a maximum of about 5 g/kg. Compared with the CRM–RAMS, the pristine ice and snow mixing ratio are about the same, the aggregates production is almost four times bigger. The decrease in ice mixing ratio near cloud base implies that this is a zone of ice crystal sublimation, that is sustained by the shape of the heating rates profile in that region. The peak in the ice mixing ratio near cloud base is associated with deep convection. Also from these time evolution figures, it can be seen that the ice production is increased during nighttime, which is consistent with *Starr and Cox (1985)* and *Akerman et al. (1988)* who found that midday cirrus were less dense than nocturnal ones and is related to radiative heating.

Snow mixing ratio (Figure 5.3 (a)) also displays three maxima - like pristine ice mixing ratio - but the main one is slightly higher. This may be due to the relatively strong and continuous ascent in the cloud.

The Turbulent Kinetic Energy (TKE) (see Figure 5.4 (a)) averaged over cloud levels exhibits some maxima associated with partial dissipation of the cirrus cloud. This occurred at 13:15 GMT (the most pronounced one), and at 18:00 and 19:00 GMT. This dissipation of the main layer of the cloud is accompanied by a small increase in the aggregate mixing ratio in the sub cloud layer. On average, the in–cloud mean TKE is about 0.3 m^2/s^2, but it depends on the grid size and domain size, since it implies an average of the total kinetic energy with respect to these two parameters. The main source for TKE production is the buoyancy term (see Figure 5.8 (a)). The reduction in the $< w'^2 >$ in the cloud layer is related to the effects of internal stabilization.

From the time evolution of TKE at all levels (Figure 5.4 (b)), we see that lower cloud layers are very active: this is the case when cumulus–like convection triggers the production or dissipation of the cirrus clouds. It is also related to the in–cloud TKE. A correlation between half vertical velocity variance $< w'^2 >$ and TKE is presented in Figure 5.5 for the last three hours of simulation, while in Figure 5.6 it is for the entire

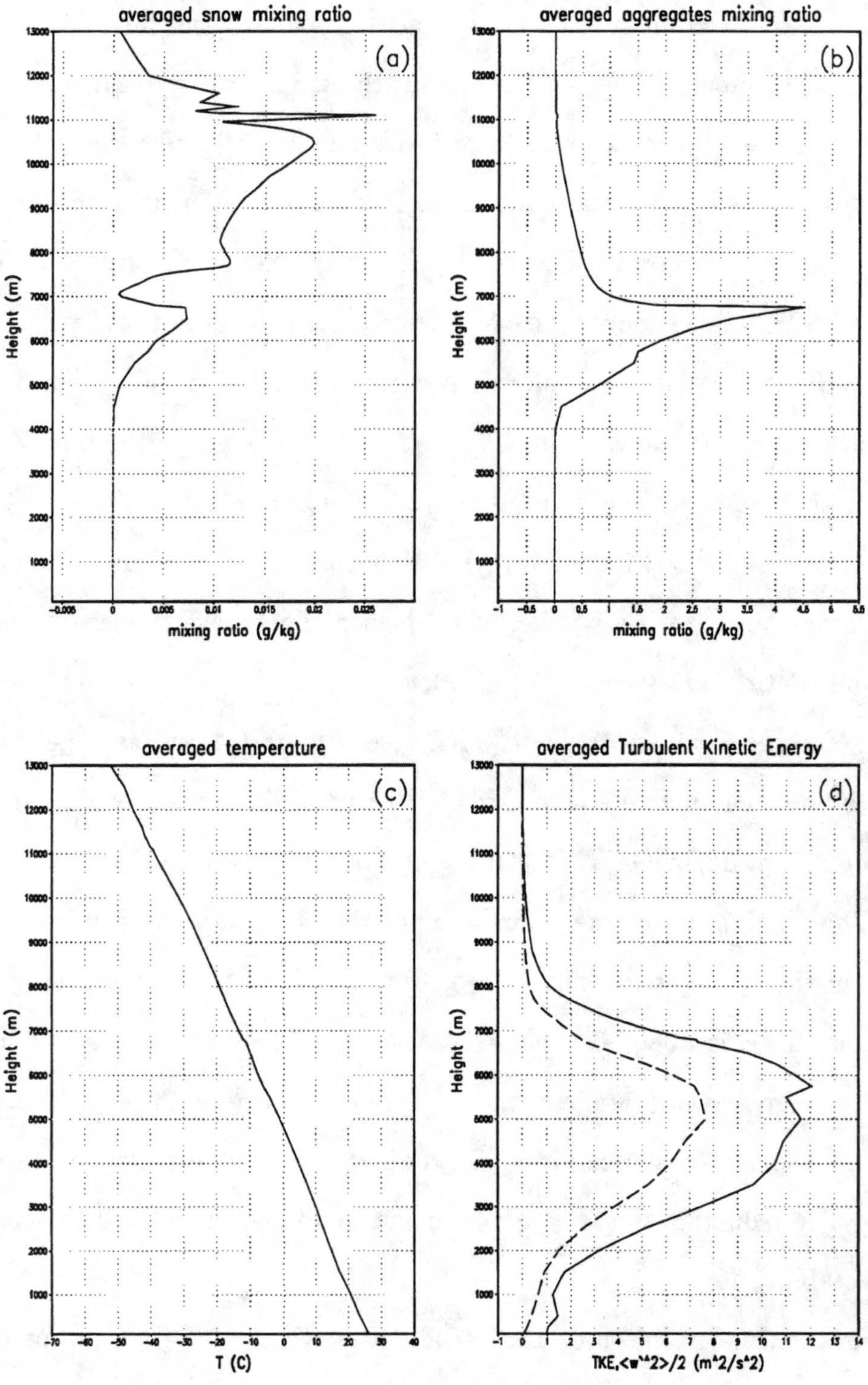

Figure 5.3: 3D simulation. (a) averaged snow mixing ratio; (b) averaged aggregates mixing ratio; (c) averaged temperature; (d) averaged TKE (solid) and half vertical speed variance (dash).

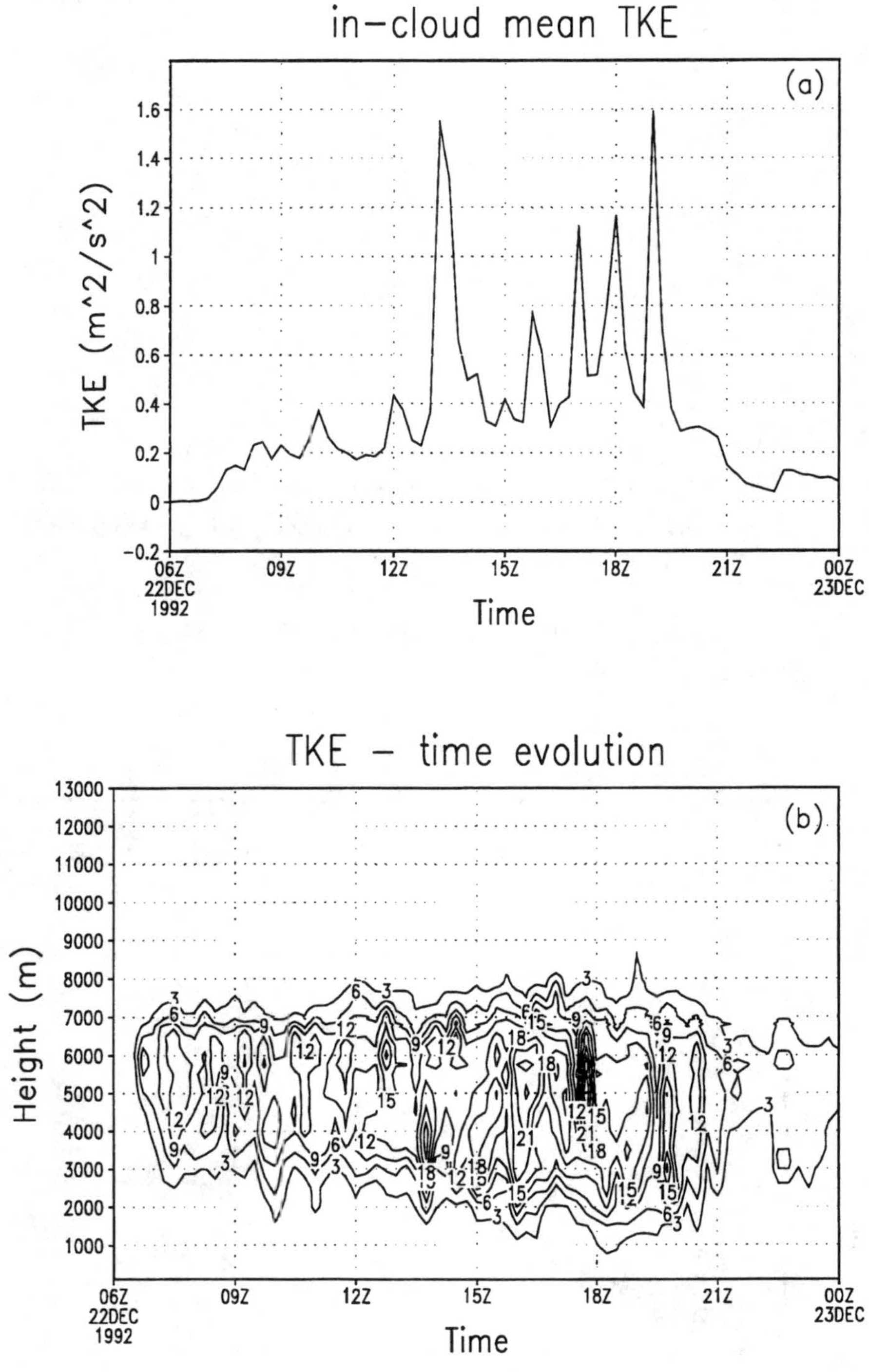

Figure 5.4: 3D simulation. (a) in–cloud TKE time evolution; (b) TKE time evolution.

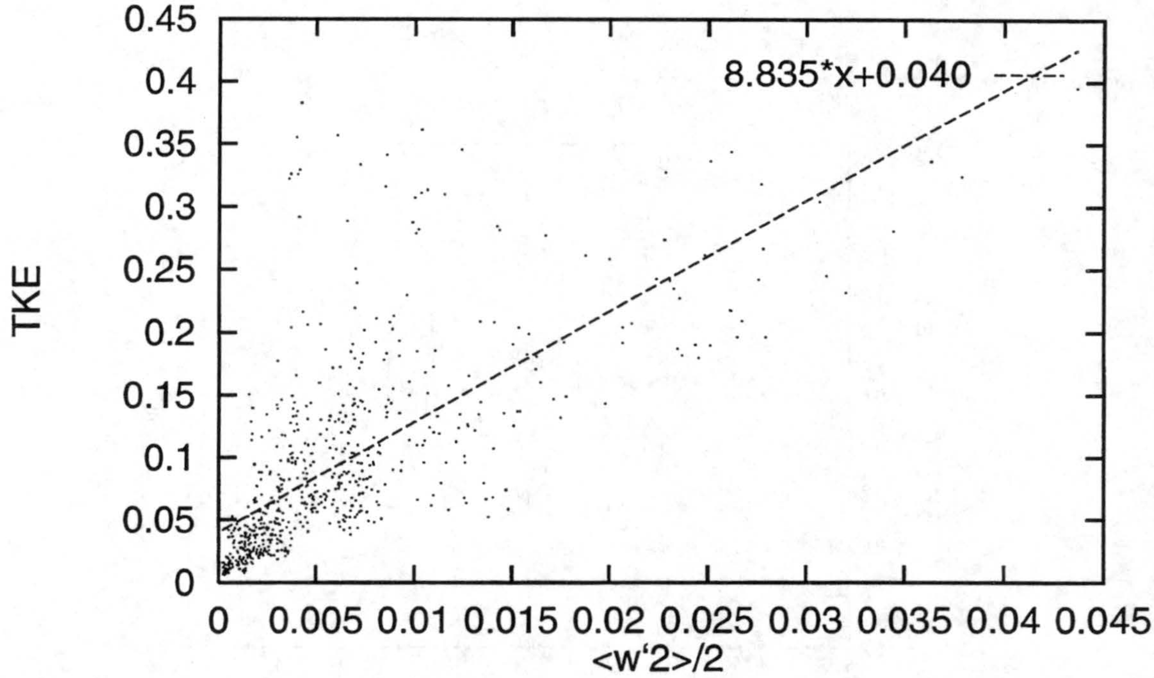

Figure 5.5: 3D simulation. TKE vs. half vertical velocity variance. Averaged between 21:00 GMT – 24:00 GMT.

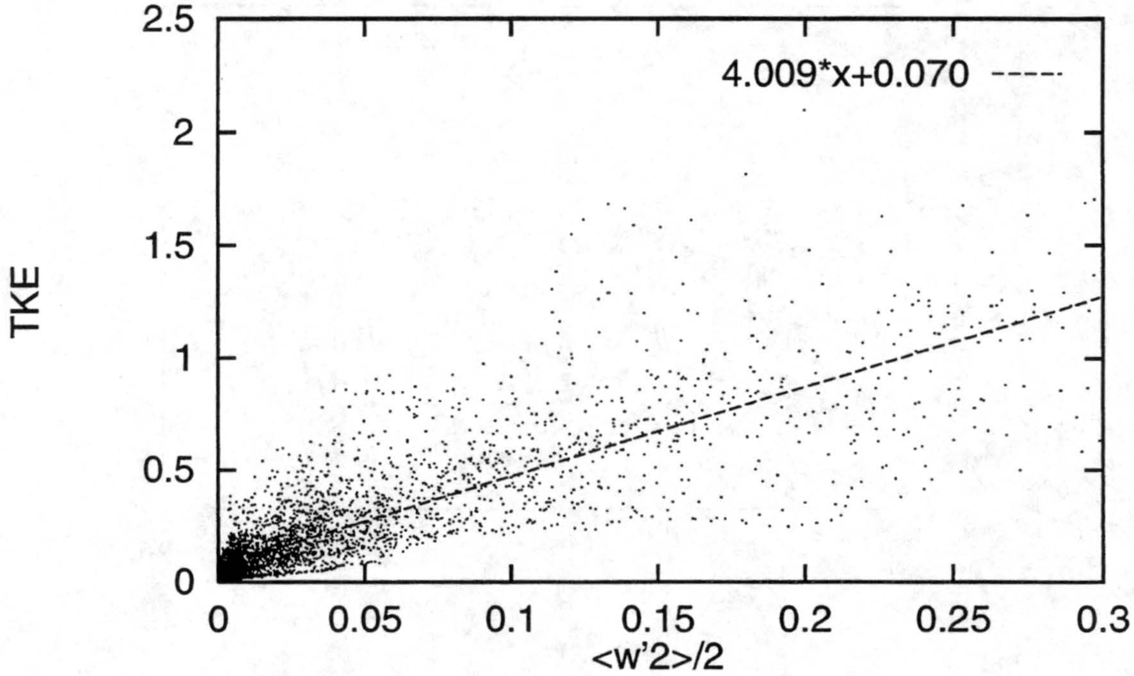

Figure 5.6: 3D simulation. TKE vs. half vertical velocity variance. Averaged between 06:00 GMT – 24:00 GMT.

time period when the in–cloud mean TKE is less than 0.3 m^2/s^2. Both figures show a relatively good correlation between these two quantities, implying that the nature of turbulence in cirrus cloud is almost two–dimensional. This is so since for the case when the deep convection is not active, the correlation coefficient is very close to nine, while for the total period is very close to four. If the nature of turbulence would have been purely three–dimensional, then the coefficient would have been exactly three, in accordance with the equipartition theorem.

As the cloud breaks up, it displays a more cellular structure as it evolves through a phase of cumulus–like activity for which entrainment is intermittent: the drying out of the layer is accomplished in intermittent bursts, which is underlined by the values of the in–cloud TKE and general feature of the TKE, and also from the skewness coefficient. Eventually, however, the cloud reforms at the same level due to the moisture flux and the cooling that exists at the top (see Figures 5.7 - 5.10).

The mean vertical velocity is positive at all levels, with a maximum of 0.27 m/s at 7000 m and then decreasing with height (Figure 5.12 (a)). But within the horizontal domain w can reach values of a couple of meters per second (see Figure 5.11), and this can also be inferred from the skewness diagram.

The skewness is a a measure of the vertical transport of the variance of w:

$$skewness = \frac{< w'^3 >}{< w'^2 >^{1.5}} \tag{5.1}$$

where $w' = w- < w >$ and $< w >$ is the mean value of w. Positive skewness implies that the updrafts are narrower and stronger. The very strong positive skewness suggests that the most efficient circulations are associated with more cumulus–like dynamics, rather than the more regular–like overturning characteristic of stratocumulus. The negative values for skewness implies that downdrafts are stronger and narrower. From Figure 5.12 (b) it can be seen that above 4500 m the mean skewness is positive, having a maximum around 6000 m, and decreasing with height. Below 4500 m it is negative, with a minimum around 3500 m. This feature implies that

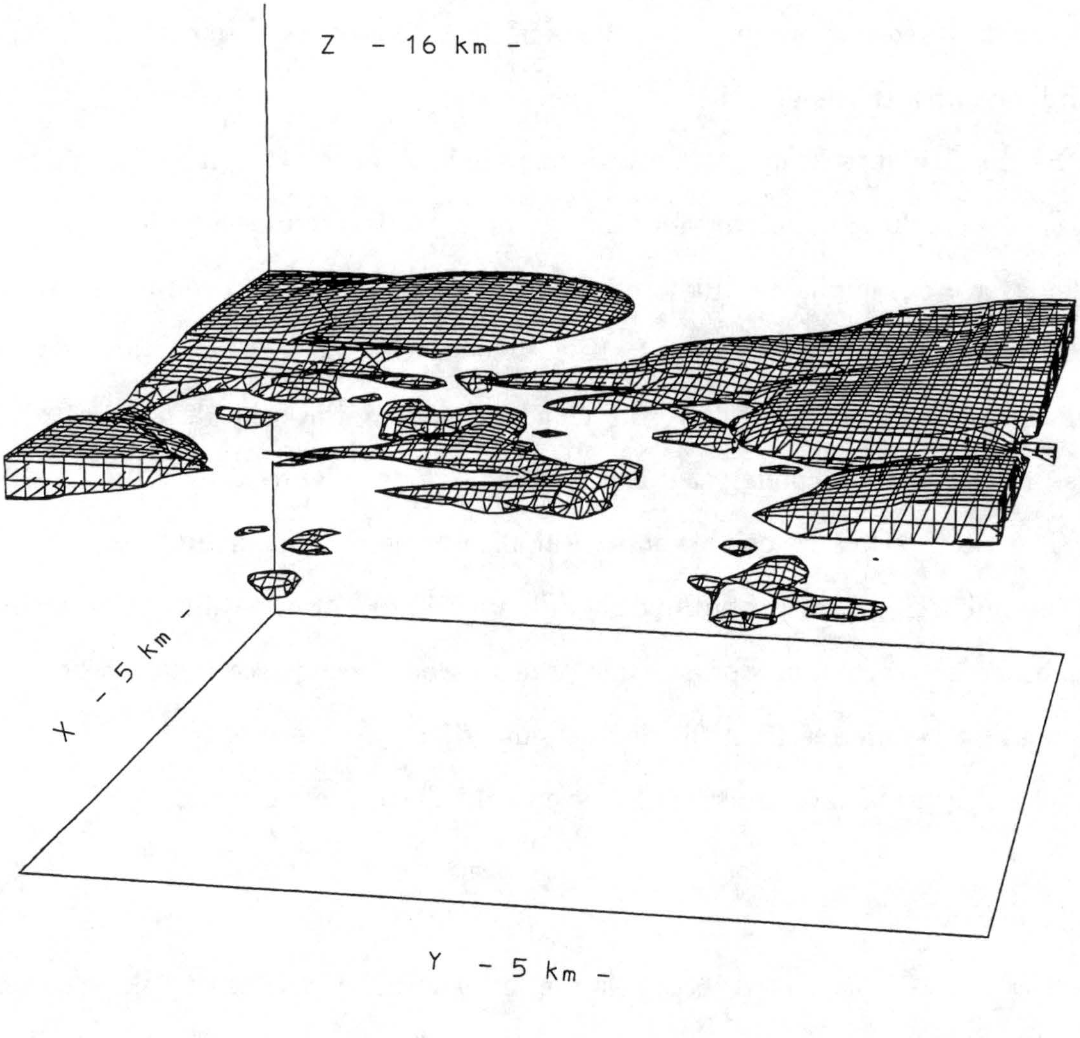

Figure 5.7: 3D simulation. Three–dimensional representation for pristine ice mixing ratio (surface for 0.15 g/kg). Time = 12:00 GMT

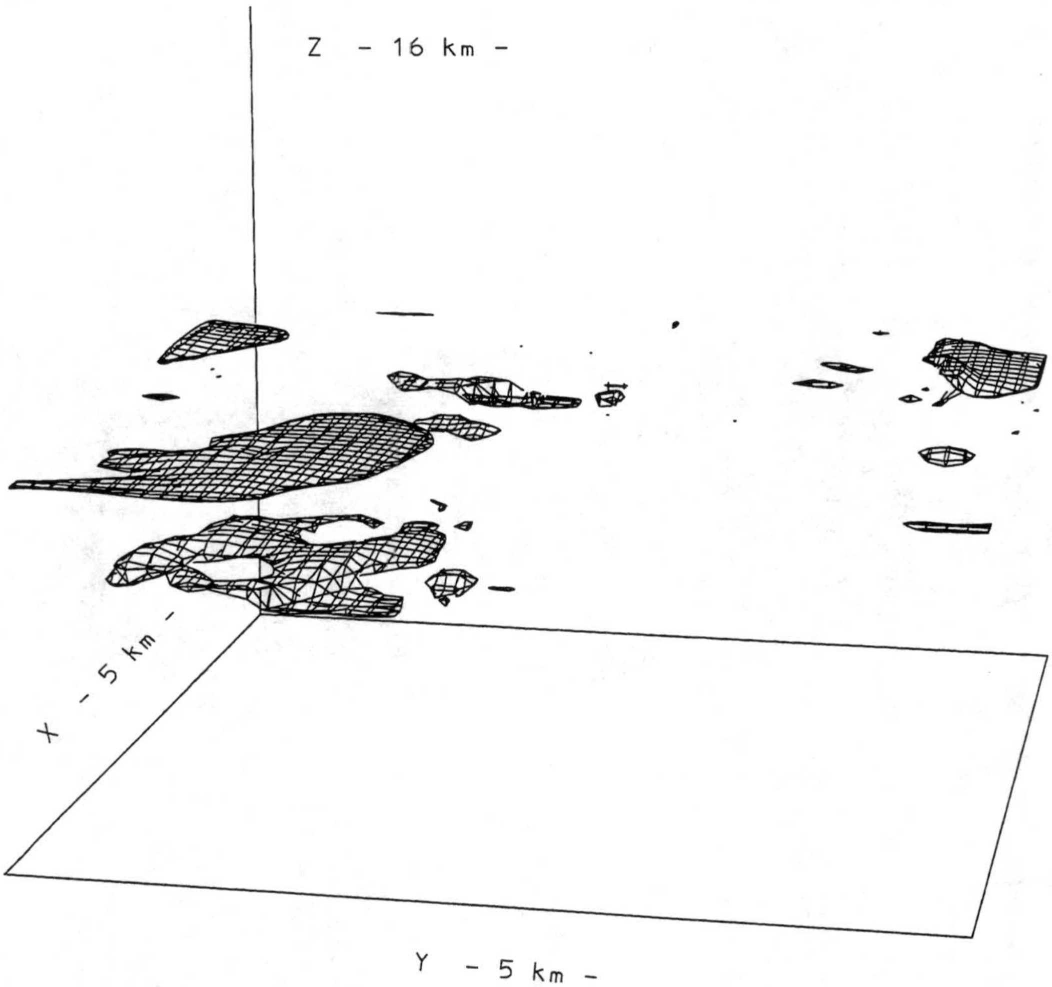

Figure 5.8: 3D simulation. Three–dimensional representation for pristine ice mixing ratio (surface for 0.15 g/kg). Time = 13:15 GMT

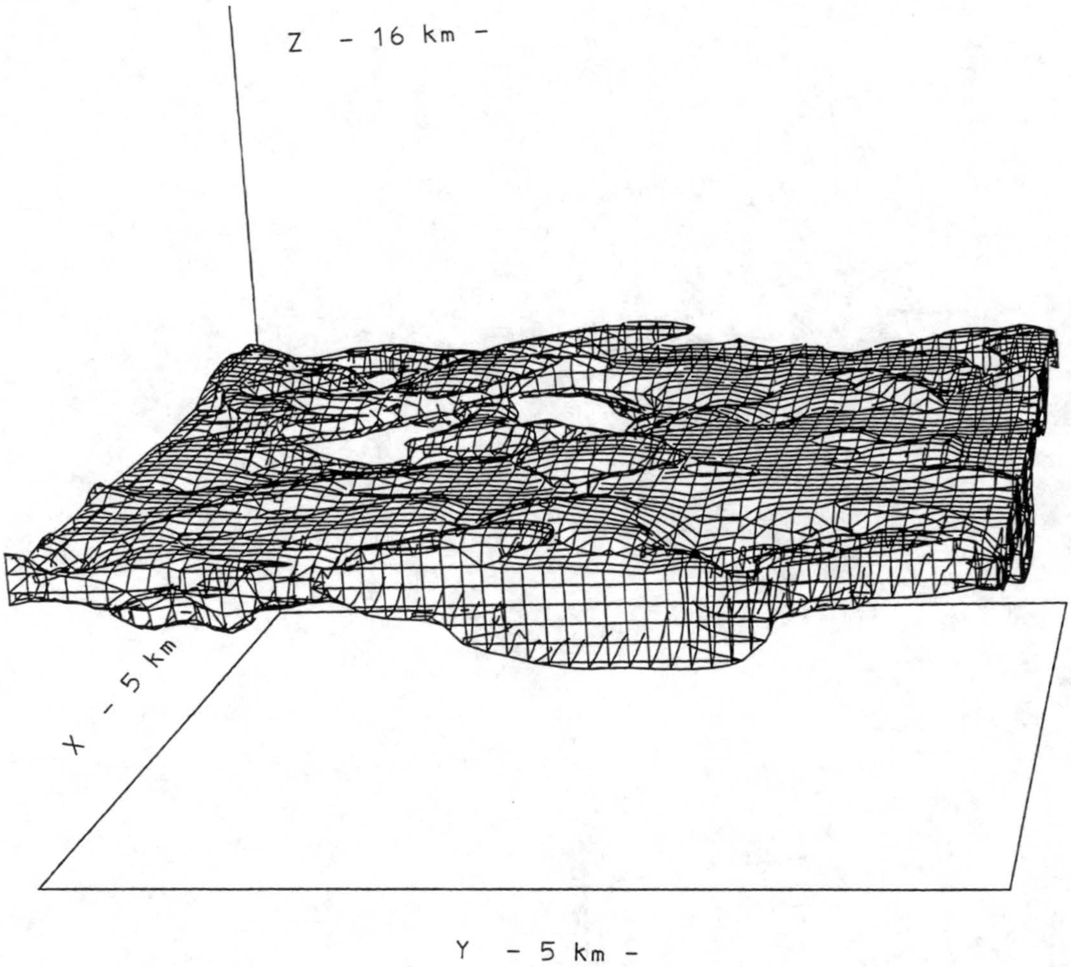

Figure 5.9: 3D simulation. Three–dimensional representation for aggregates mixing ratio (surface for 1.1 g/kg). Time = 12:00 GMT

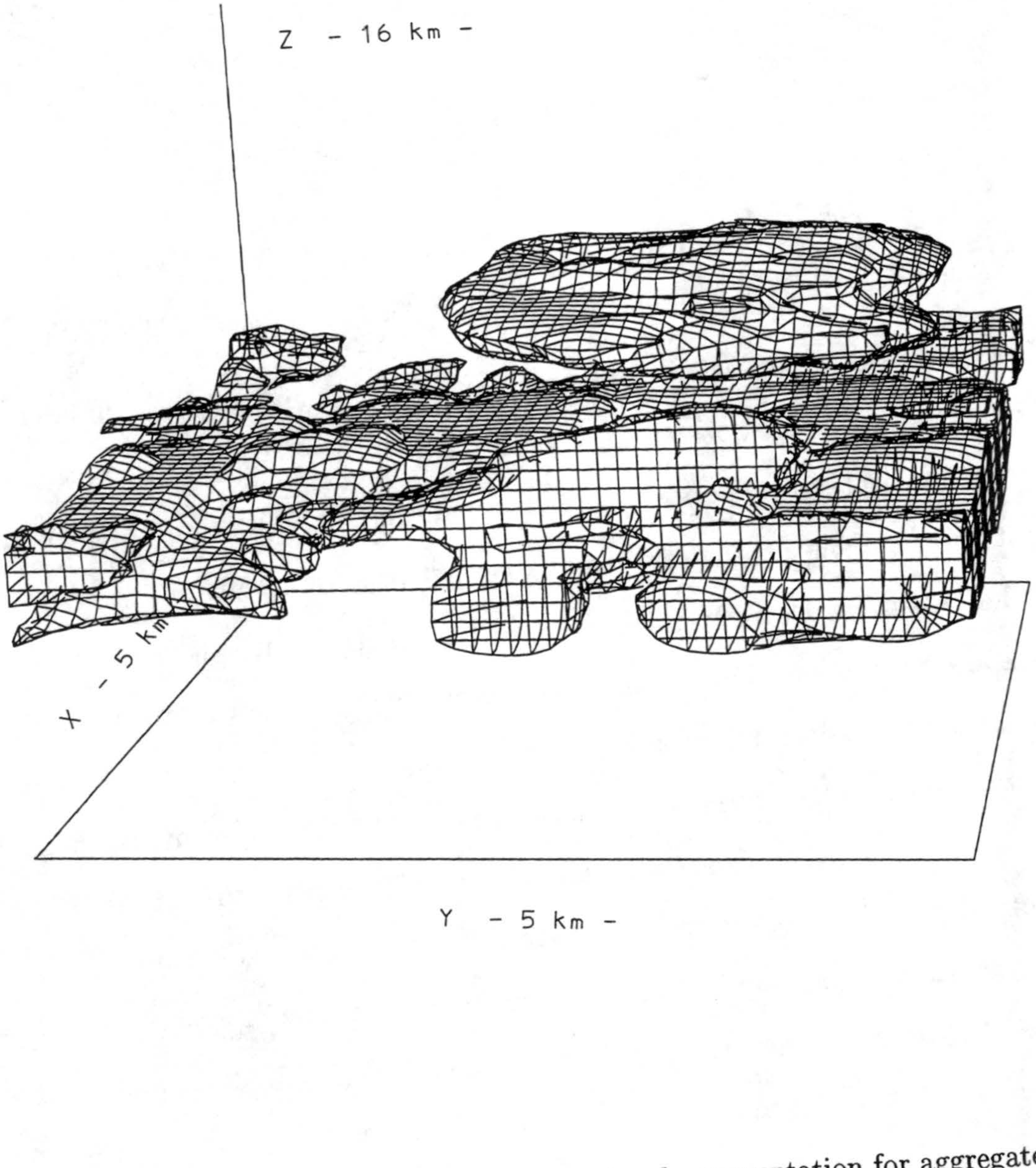

Figure 5.10: 3D simulation. Three–dimensional representation for aggregates mixing ratio (surface for 1.1 g/kg). Time = 13:15 GMT

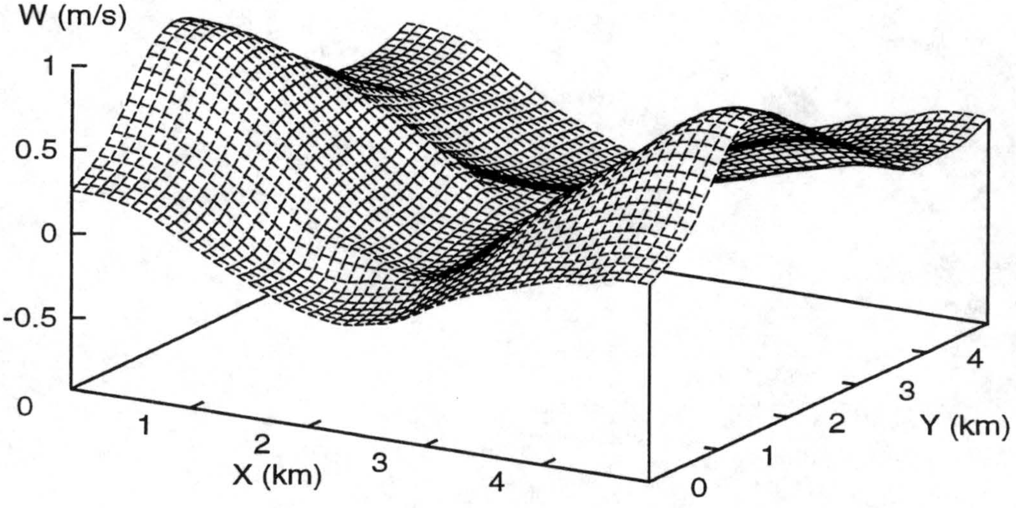

Figure 5.11: 3D simulation. w variation at 9500 m. Time = 12:00 GMT

turbulence is very active below cloud base, but still has some contribution in cloud, and cumulus–like circulations are the predominant feature. But at some moments, skewness can display an opposite feature. This may happen after precipitation occurs, since it is accompanied by narrow and relatively strong downdrafts.

The heating and cooling rates obtained for this case with the new radiation module are very close to those obtained from other models and/or measurements. In Figure 5.12 (c), the dotted line represents the heating rates profile as an average over the last three hours (i.e. during daytime), while the solid line represents the heating rate profile as averaged over the entire time of simulation. During the day (see Figure 5.12 (c) - dotted line), due to the SW absorption, the heating rates are larger than those obtained from averaging over the entire time of simulation (solid line, same figure). The increase is the largest at the top of the cloud (5–7 K/day), while for the lower regions is about 2 K/day. At the top of the cloud, the infrared radiative cooling dominates, having a peak around -15 K/day. This value is very close to that obtained by *Griffith et al. (1980)* using a broadband infrared radiative transfer model and is within the range of various other models. This is mainly due to the relatively small crystals (pristine ice), since the snow and aggregates crystals concentrations are low

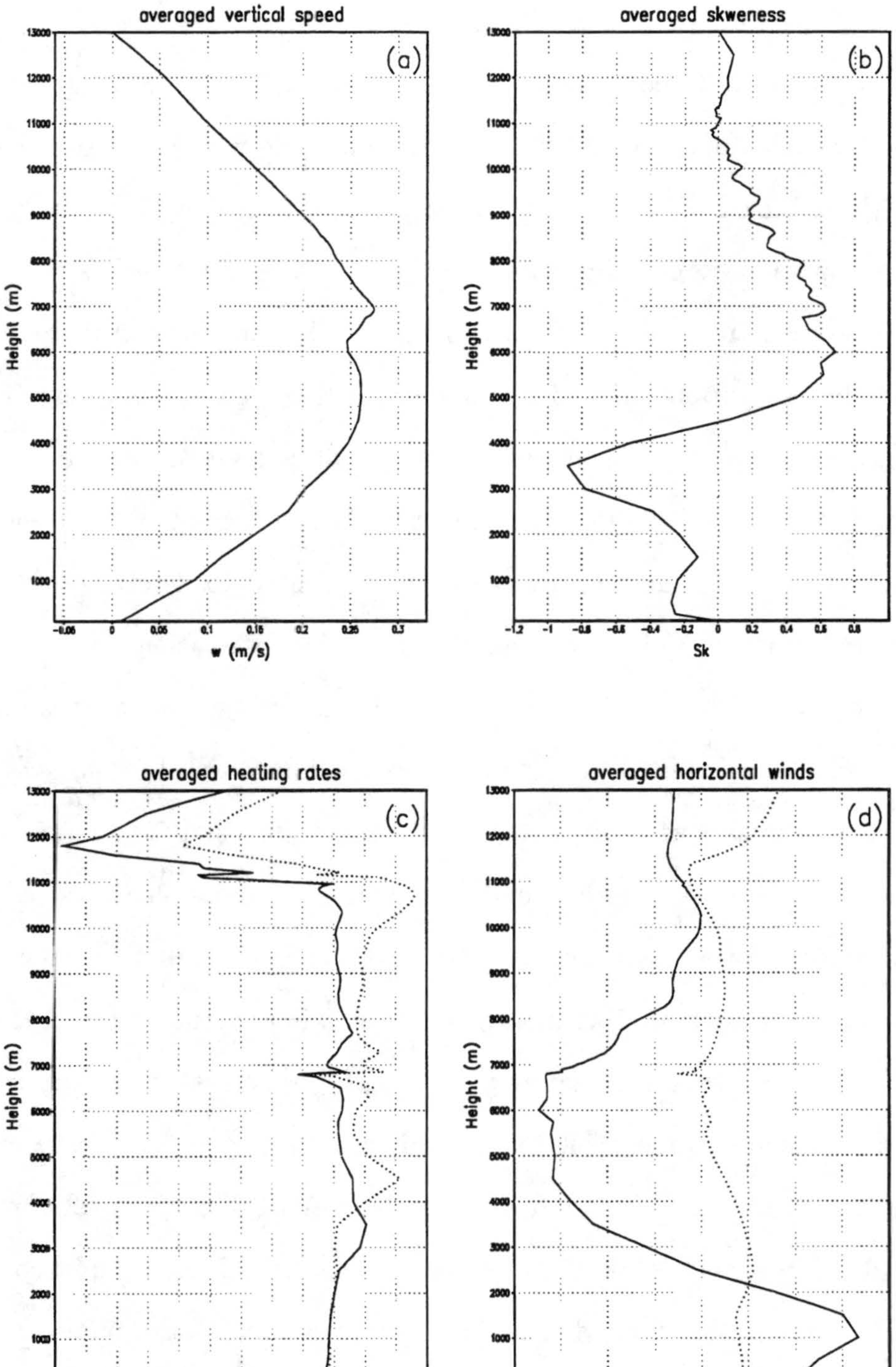

Figure 5.12: 3D simulation. (a) averaged vertical velocity; (b) averaged skewness; (c) averaged heating rates (18 hours average - solid, last 3 hours average - dots); (d) averaged horizontal winds (U - solid, V - dots).

at this altitude, combined with the higher total surface area that small particles have compared with larger ice crystals having the same mass. For the subcloud region, the typical profile that accompanies latent heat phase changes occurs. At sea level the cooling rate is about -3 K/day, a value comparable with that obtained by *Liou (1986)*. Above the cloud, the cooling rate increases with height due to carbon dioxide and ozone emission. According to a study by *Zender and Kiehl (1994)*, optically thick clouds are characterized by sharp changes in flux profiles and therefore a small change in the absorption properties of a given distribution of condensate can result in significant local changes in heating rates. Small crystals are also responsible for increasing total absorption, while treating crystals as hexagons this may be reduced. The conclusion is that the flux divergence may be used to determine what crystal size, or shape or both need to be tuned to match the observations.

From the mean horizontal winds (Figure 5.12 (c)) we see that the mean horizontal U–component of the wind is westerly - with a maximum speed of 4.5 m/s at about 1000 m, then decreases with height to a minimum of -9 m/s at 6000 m and after that a decrease to -2 m/s. Above the cloud, the value is at about -3.5 m/s. Although it displays a strong shear, shear production of TKE is almost negligible when compared with buoyancy production. But this strong mean wind ventilates the ocean surface, and this can be seen from the heating rates profile, an increase in the surface sensible heat, and also maintain more TKE in the sub–cloud layer.

The pristine ice, snow and graupel vertical fluxes are displayed in Figure 5.13 (a), (c) and (d) respectively, while the pristine ice horizontal flux is displayed in Figure 5.13 (b). For computing these fluxes, the Reynolds average was applied:

$$<AB> = <A><B> + <A'B'>$$

where A stands for velocity (vertical velocity for the vertical fluxes or horizontal velocity for the horizontal flux), and B is the mixing ratio of the various hydrometeors.

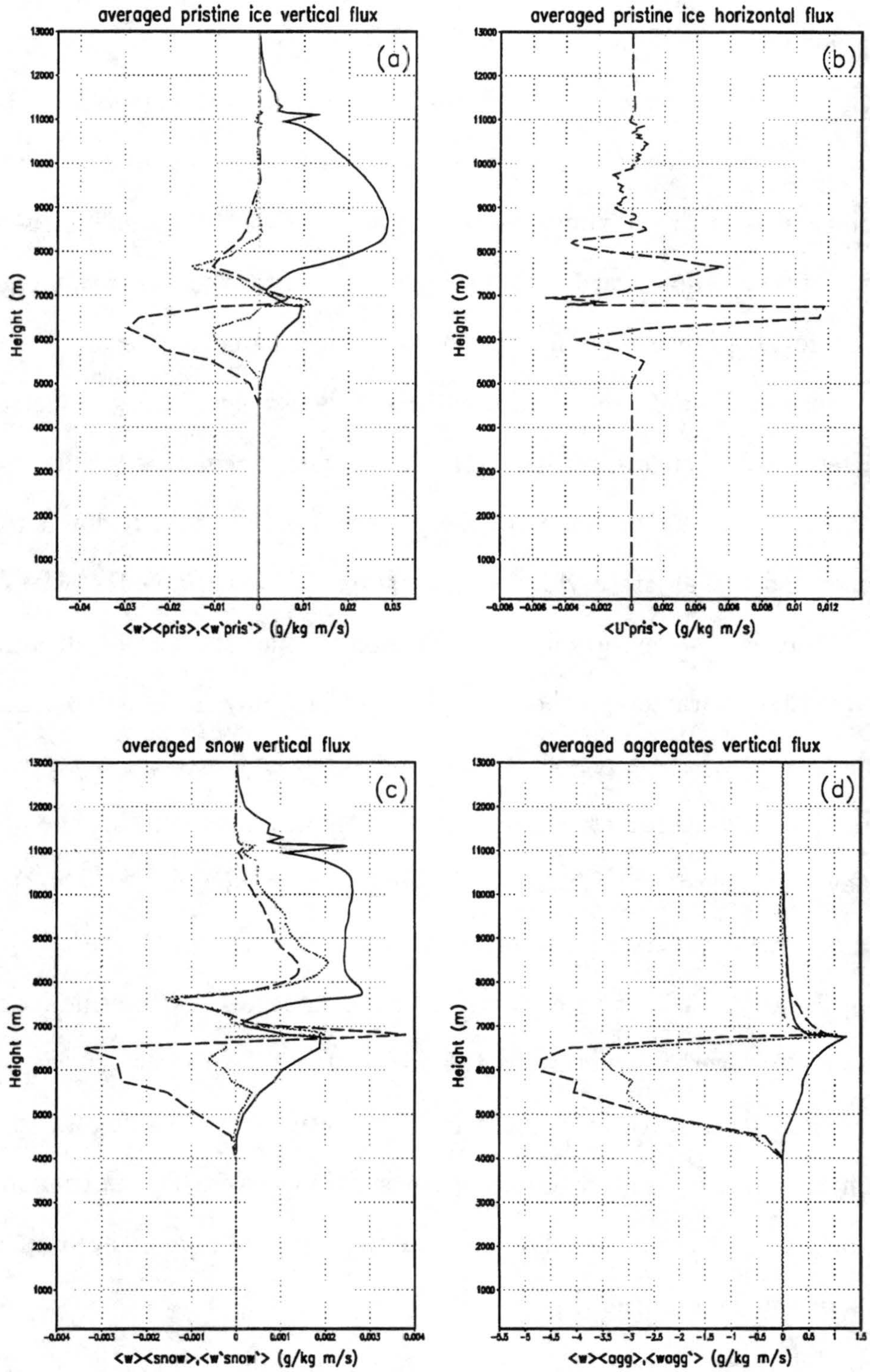

Figure 5.13: 3D simulation. (a) pristine ice averaged vertical flux (mean flux - solid, upward - dash, downward - dots); (b) pristine ice averaged horizontal flux (mean flux - solid, upward - dash, downward - dots); (c) snow averaged vertical flux (mean flux - solid, upward - dash, downward - dots); (d) aggregates averaged vertical flux (mean flux - solid, upward - dash, downward - dots).

The term $< A'B' >$ can also be decomposed into contributions according to the vertical velocity sign (upward or downward fluxes).

From the pristine ice and snow fluxes, we see that in the cloud layer the fluxes are positive (upward) having a maximum at about 9000 m for pristine ice and snow which coincides with the maximum in the mixing ratio distribution. For the subcloud region the fluxes are downward with a strong gradient for the separation region. The flux for aggregates is very low for the in–cloud region due to the low values of the mixing ratio, but for the subcloud layer the flux is downward and very strong. The same pattern with a strong gardient for the separation region is visible. Whenever there is a maximum or a minimum in the pattern of a flux, that region is a region of convergence and is characterized by a steady state for the variable that gives the flux; whenever there is a strong gradient that region is characterized by divergence and the variable that characterizes the flux may grow or decay in time depending on the sign of the gradient. These regions are in good agreement with the observed maxima and minima for the hydrometeors mixing ratio vertical distribution. The presence of the dry layer is consistent with *Heymsfield and McFarquhar (1996)* who showed the existence of a dry layer near cloud base where ice particles sublimate.

From Figure 5.13 (b) which shows the horizontal flux for pristine ice it can be clearly seen the layered structure of the cirrus cloud - especially at the bottom of the main cloud layer, with layers that move horizontally with different speeds, and that the horizontal flux is more intense in the subcloud layer. This particular pattern, however may be a result of the relatively limited horizontal domain accompanied with the cyclic boundary conditions.

A special interest is the Probability Distribution Function (PDF) for vertical velocity, since knowledge about this parameter can be useful in one–dimensional models for parameterization of cloud microphysics. Following the definition of a PDF:

$$PDF(w) = \frac{dN(w)}{dV\,dw} \tag{5.2}$$

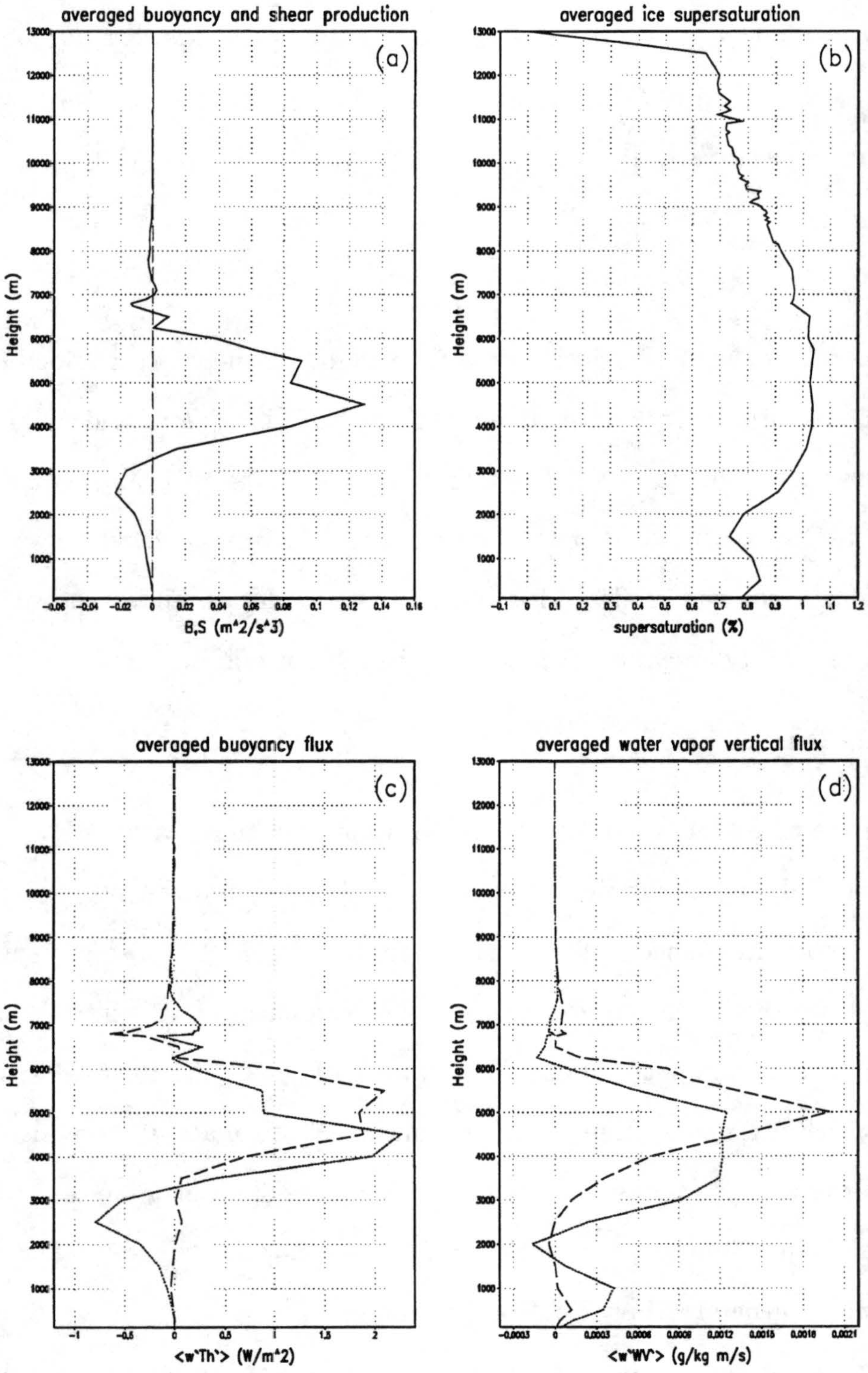

Figure 5.14: 3D simulation. (a) averaged buoyancy (solid) and shear (dash) production; (b) averaged ice supersaturation; (c) averaged buoyancy flux (upward - dash, downward - dots); (d) averaged water vapor vertical flux (upward - dash, downward - dots).

where $dN(w)$ represents the elementary volume of fluid with speeds in the interval $w \pm dw$, dV is the total volume and dw is speed threshold, the PDF was computed in the interval -5, +5 m/s (which covers almost the entire vertical velocity spectra). In a first approximation to the computed PDF, a Gaussian function of probability was tested:

$$GDF(w) = \frac{1}{\sqrt{2\pi}\sigma} exp\left(-\frac{(w - < w >)^2}{2\sigma^2}\right) \tag{5.3}$$

where $< w >$ is the mean velocity, σ^2 is the variance of the vertical velocity. Because the Gaussian probability distribution function (GDF) is a symmetric one, it does not have skewness (skewness = 0). In Figures 5.15 – 5.18 the PDF along with GDF are represented. We can see that the approximation is very good, although the PDF shows some secondary modes. These peaks may not play an important role since the updraft variability is relatively small (less than $\pm$ 1 m/s).

5.3 2D Run

For the two–dimensional run, the same graphs, but those with PDF are provided. Like for the 3D run, the two cloud layers are visible, but now the interaction between layers is more pronounced. This is visible from Figures 5.20 (b) and 5.22 (b) from which we see that deep convection is responsible for penetrating into the top layer. In this case the main penetrations occur at about 11:45 GMT, 19:45 GMT and 21:15 GMT, which is different from the three–dimensional simulation. Note also the large values for the in–cloud mean TKE which for the times of penetration can reach values between 12 and 23 m^2/s^2, as well as the TKE that now has greater values and more turbulence is generated in the bottom cloud layer.

Due to the more active dynamics the mixing ratios are higher: pristine ice has maximum values of about 0.16 g/kg (Figure 5.19 (b)) and aggregates mixing ratios can reach as much as 6 g/kg (Figure 5.20 (b)). The vertical profiles of the distribution remain basically the same as in the three–dimensional run.

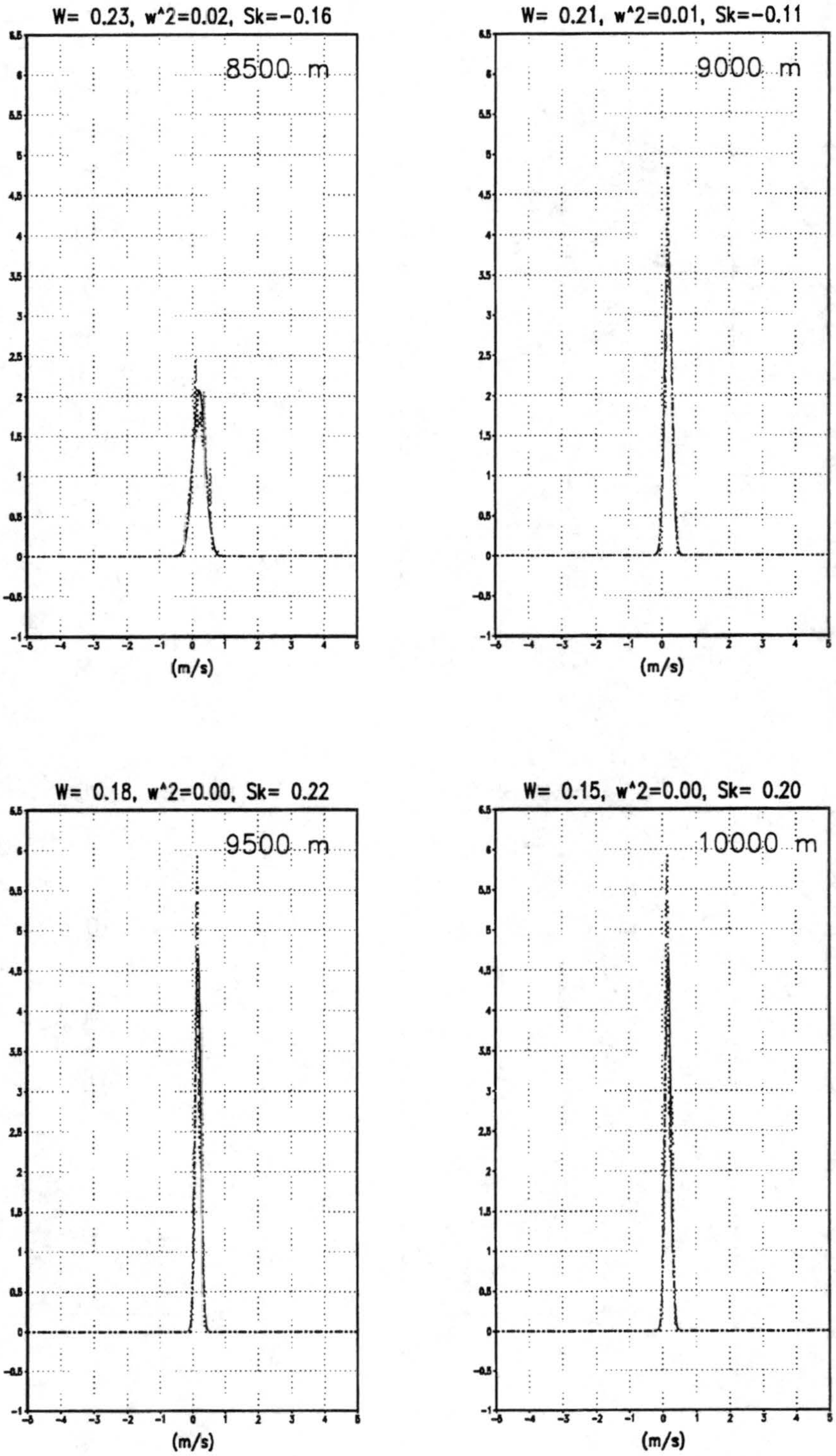

Figure 5.15: 3D simulation. GDF (solid) and PDF (dash) at time 11:00 GMT. Mean velocity (W), variance (w2) and skewness (Sk) are listed.

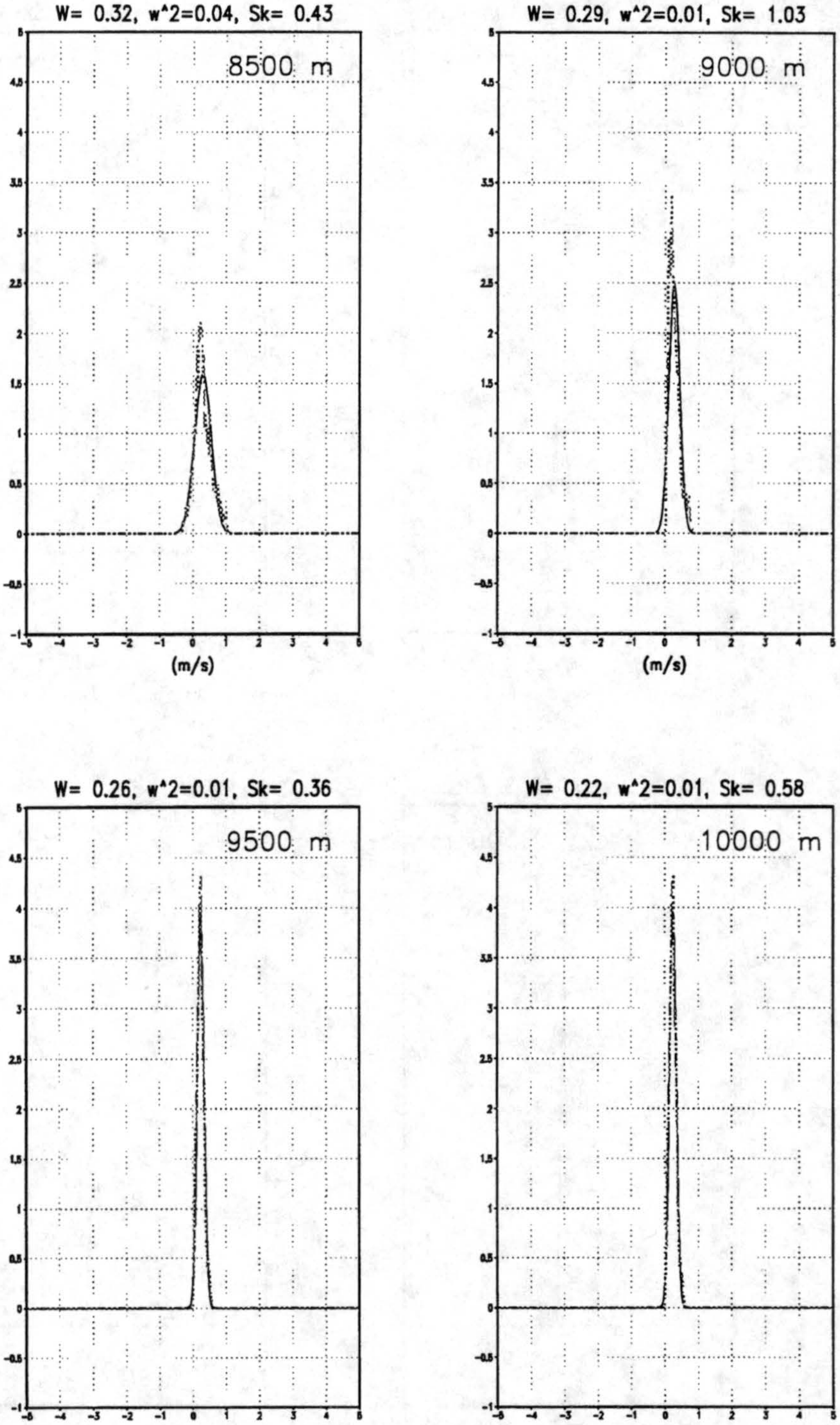

Figure 5.16: 3D simulation. GDF (solid) and PDF (dash) at time 11:30 GMT. Mean velocity (W), variance (w2) and skewness (Sk) are listed.

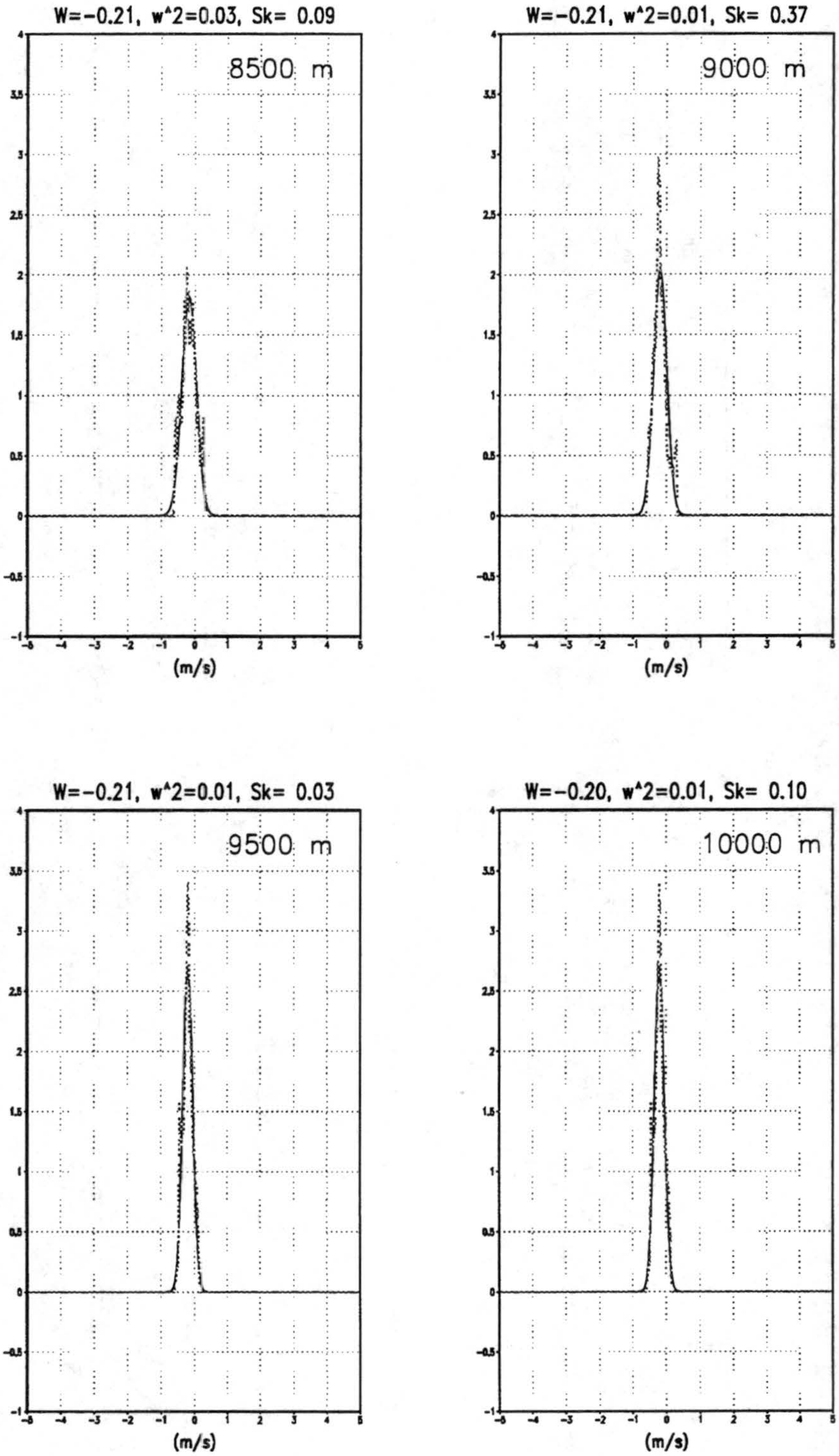

Figure 5.17: 3D simulation. GDF (solid) and PDF (dash) at time 21:00 GMT. Mean velocity (W), variance (w2) and skewness (Sk) are listed.

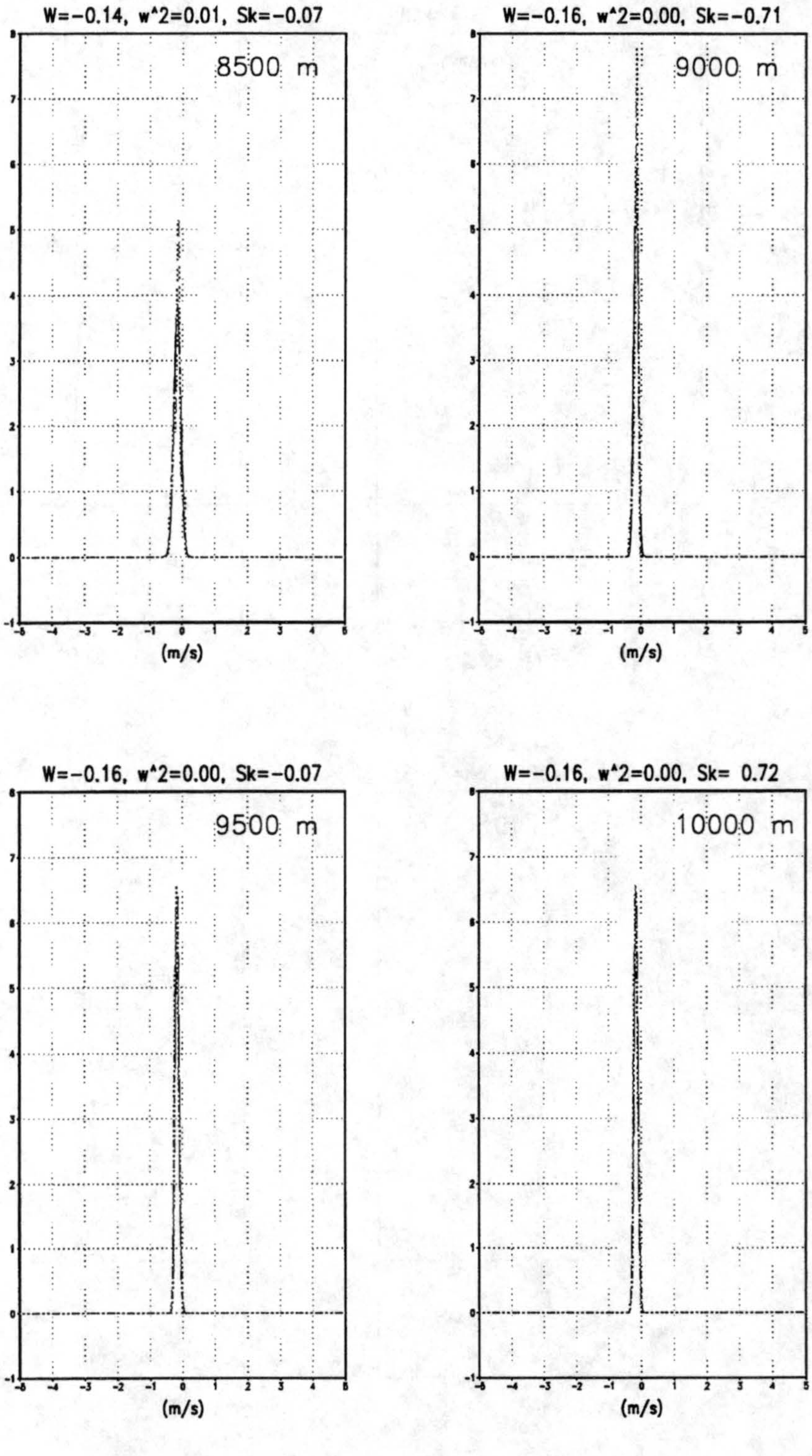

Figure 5.18: 3D simulation. GDF (solid) and PDF (dash) at time 21:30 GMT. Mean velocity (W), variance (w2) and skewness (Sk) are listed.

The hydrometeors fluxes (Figures 5.24 (a),(c),(d)) shows a larger vertical transport in the top layer cloud especially for the aggregates. The layered structure of the top cloud layer is now more pronounced according to Figure 5.24 (b).

5.4 Comparison with a mid–latitude cirrus run

Wu (1998) using the RAMS two–moment scheme that uses prognostic equations for both concentrations and mixing ratios for pristine ice, snow and aggregates, in an Large Eddy Simulation configuration. He simulated the early stages of mid–latitude cirrus clouds over a 60x40x140 grid size domain with horizontal grid spacing set to 100 m and variable vertical spacing levels up to 12400 m. At cirrus cloud levels the vertical spacing is 50 m. The region over which the simulation took place is at 37.79°N and 97.24°W. With a time step of 1 second, after two hours of simulation and using nudging files, the spatial distribution for pristine ice, snow and aggregates mixing ratios are plotted in Figures 5.26, 5.27 and 5.28 respectively.

According to these figures, the mixing ratio for pristine ice is about 0.02 g/kg at about 9500 m, for snow 0.14 g/kg at 7800 m and 0.17 g/kg at 4000 m for aggregates. These values are different from the tropical case in the sense that the values with the exception of snow are much smaller. Also it can be inferred that for mid–latitude cirrus there are more large ice crystals. The vertical velocity field has a magnitude of 0.24 m/s (comparable with the tropical run), but it doesn't exhibit a cumulus–like circulation.

5.5 Comparison with a precipitating stratocumulus

In a study by *Stevens (1996)* concerning the effects of drizzle in a stratocumulus cloud, the conclusion was that drizzle has the effect of stabilizing the sub–cloud layer with respect to the cloud layer and that the cooling of the sub–cloud layer can destabilize it with respect to the surface. When drizzle is reduced, entrainment warms

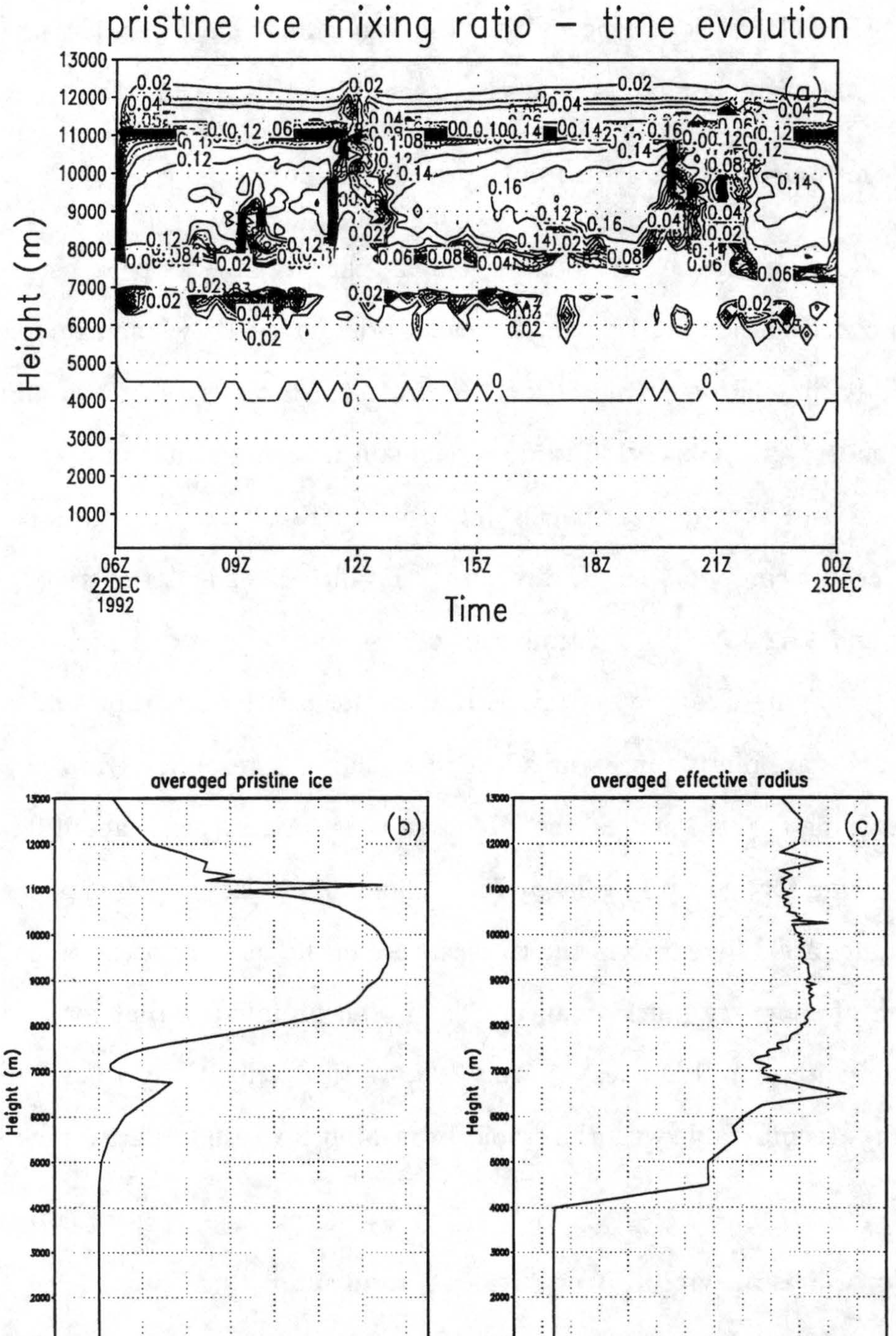

Figure 5.19: 2D simulation. (a) pristine ice mixing ratio time evolution; (b) averaged pristine ice mixing ratio distribution; (c) averaged pristine ice effective radius distribution.

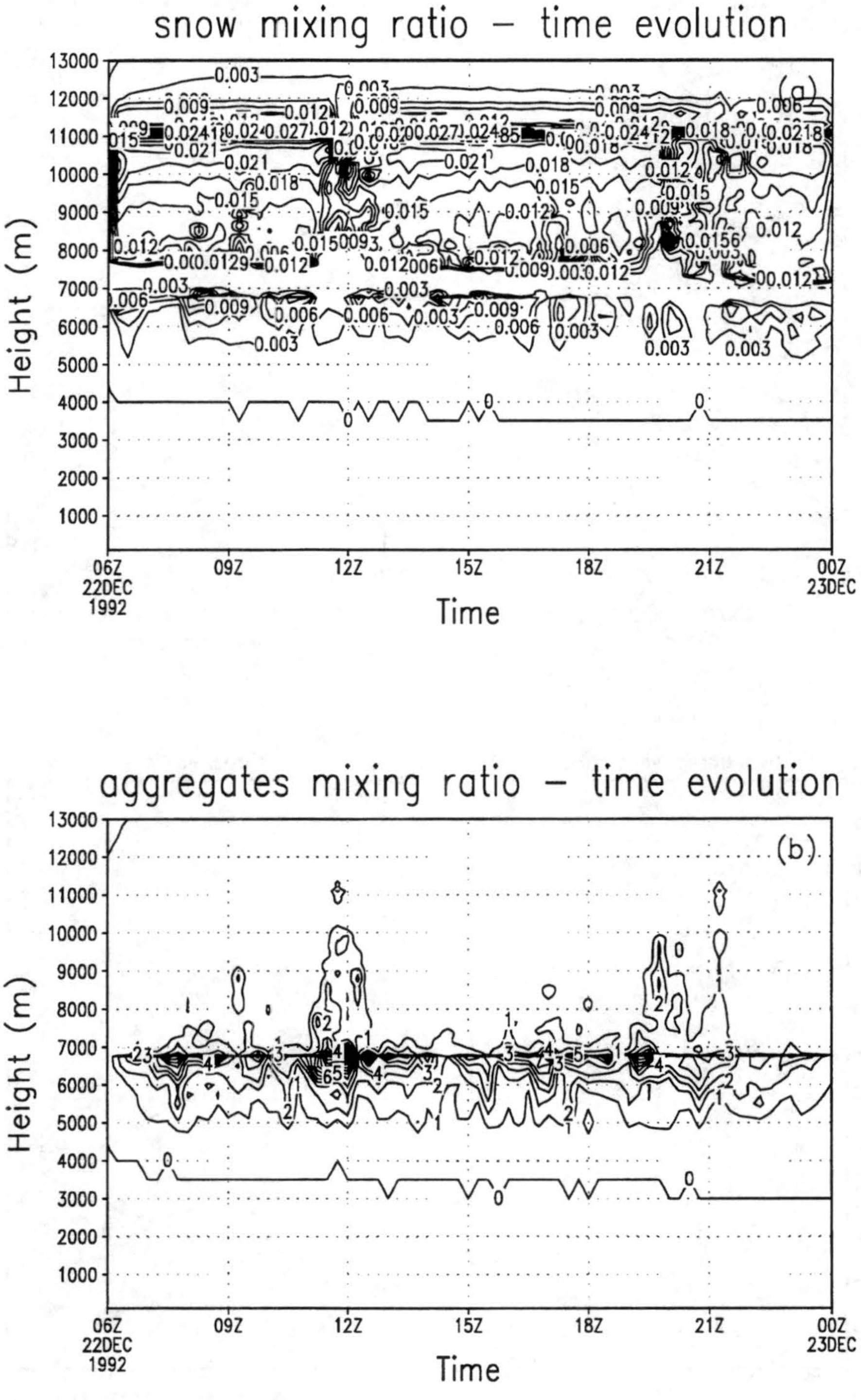

Figure 5.20: 2D simulation. (a) snow mixing ratio time evolution; (b) aggregates mixing ratio time evolution.

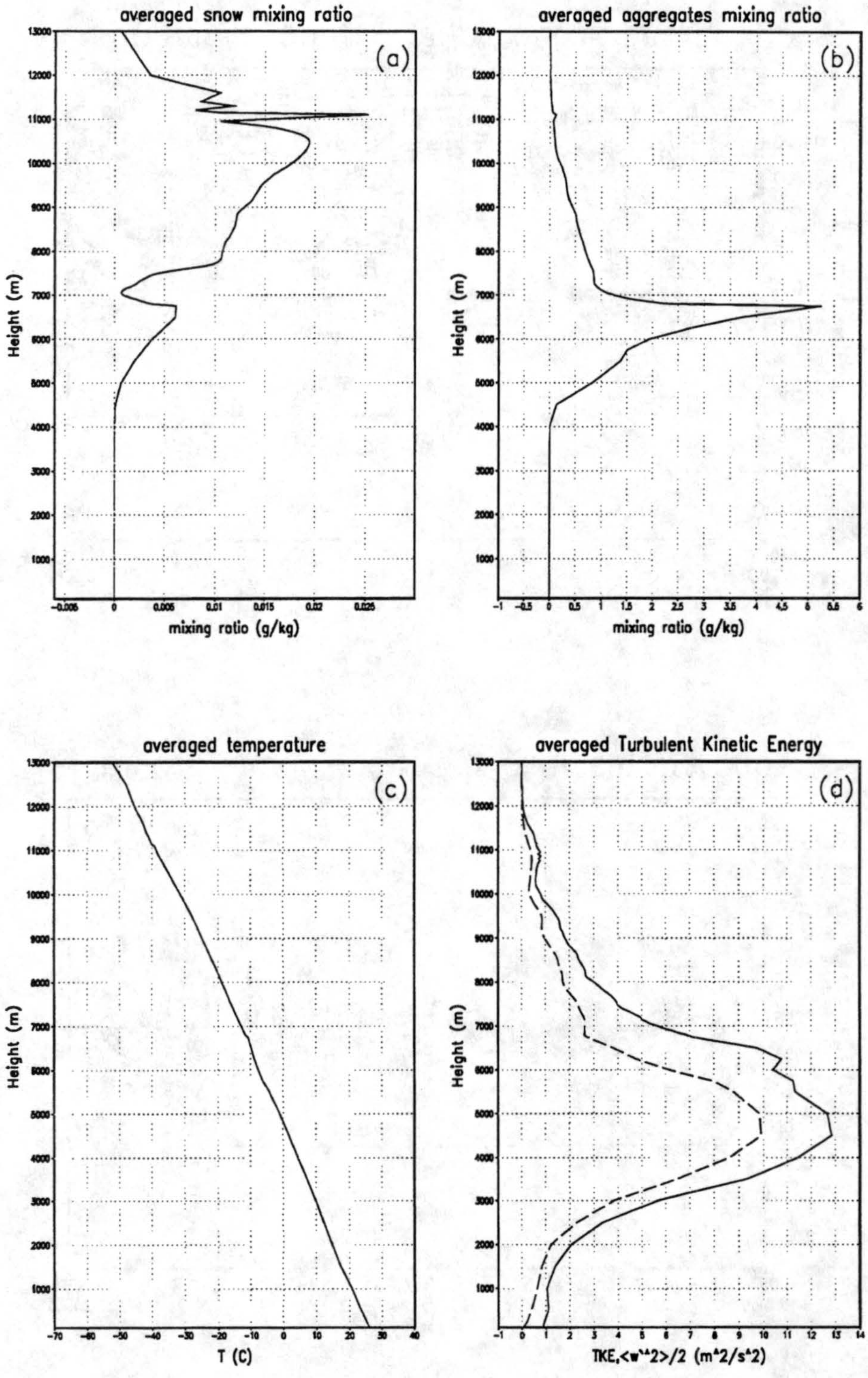

Figure 5.21: 2D simulation. (a) averaged snow mixing ratio; (b) averaged aggregates mixing ratio; (c) averaged temperature; (d) averaged TKE (solid) and half vertical speed variance (dash).

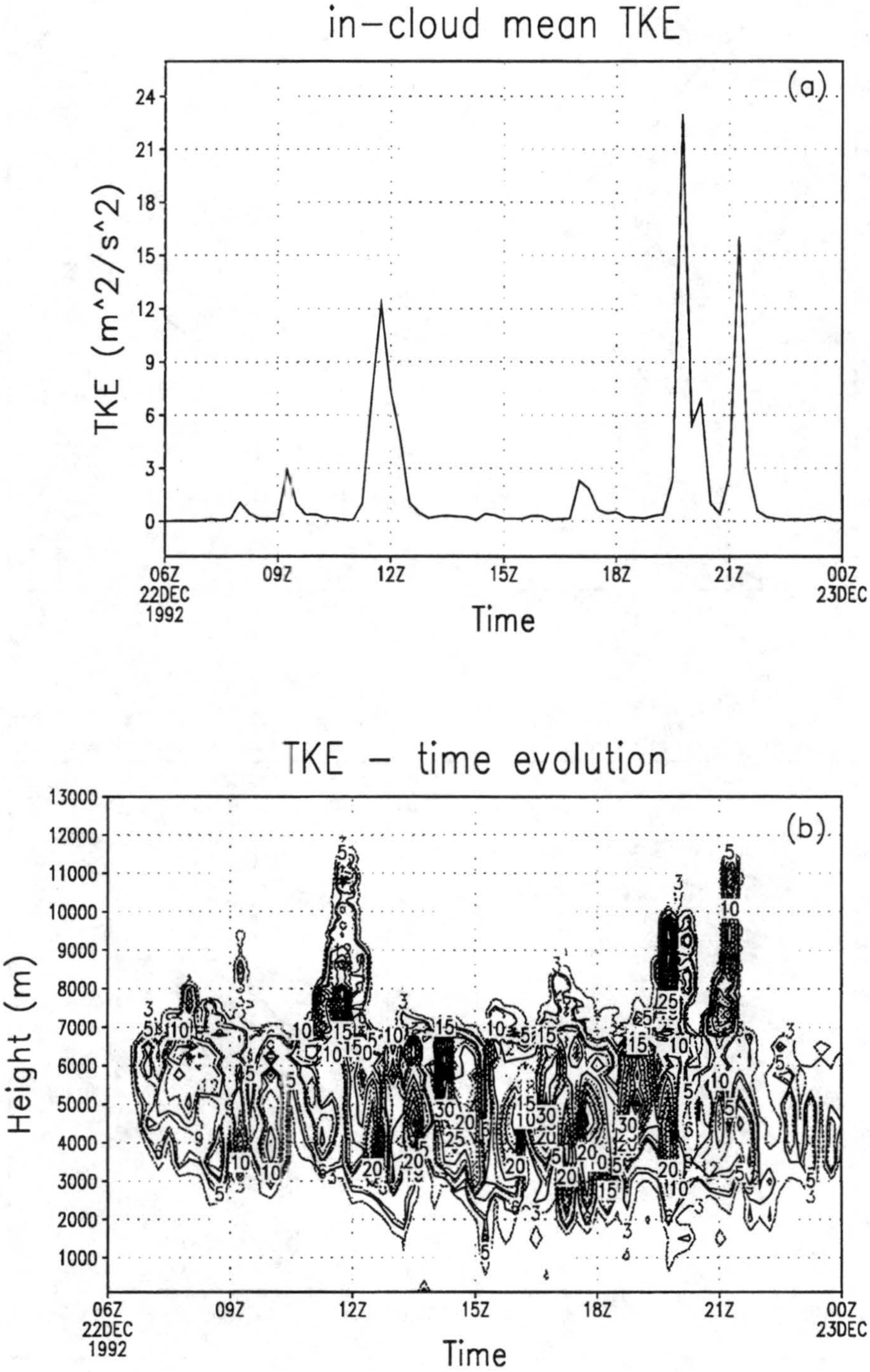

Figure 5.22: 2D simulation. (a) in–cloud TKE time evolution; (b) TKE time evolution.

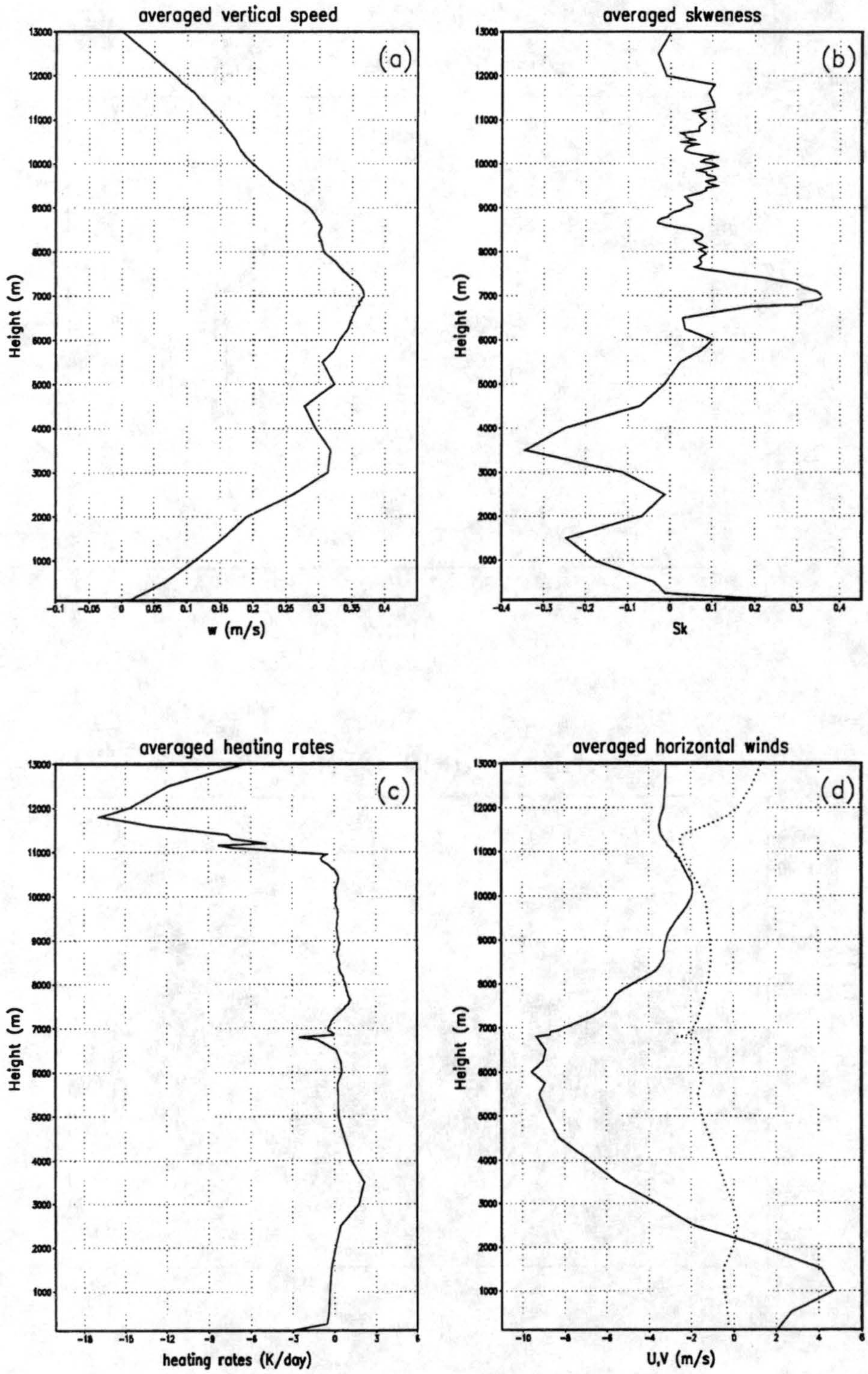

Figure 5.23: 2D simulation. (a) averaged vertical velocity; (b) averaged skewness; (c) averaged heating rates; (d) averaged horizontal winds (U - solid, V - dots).

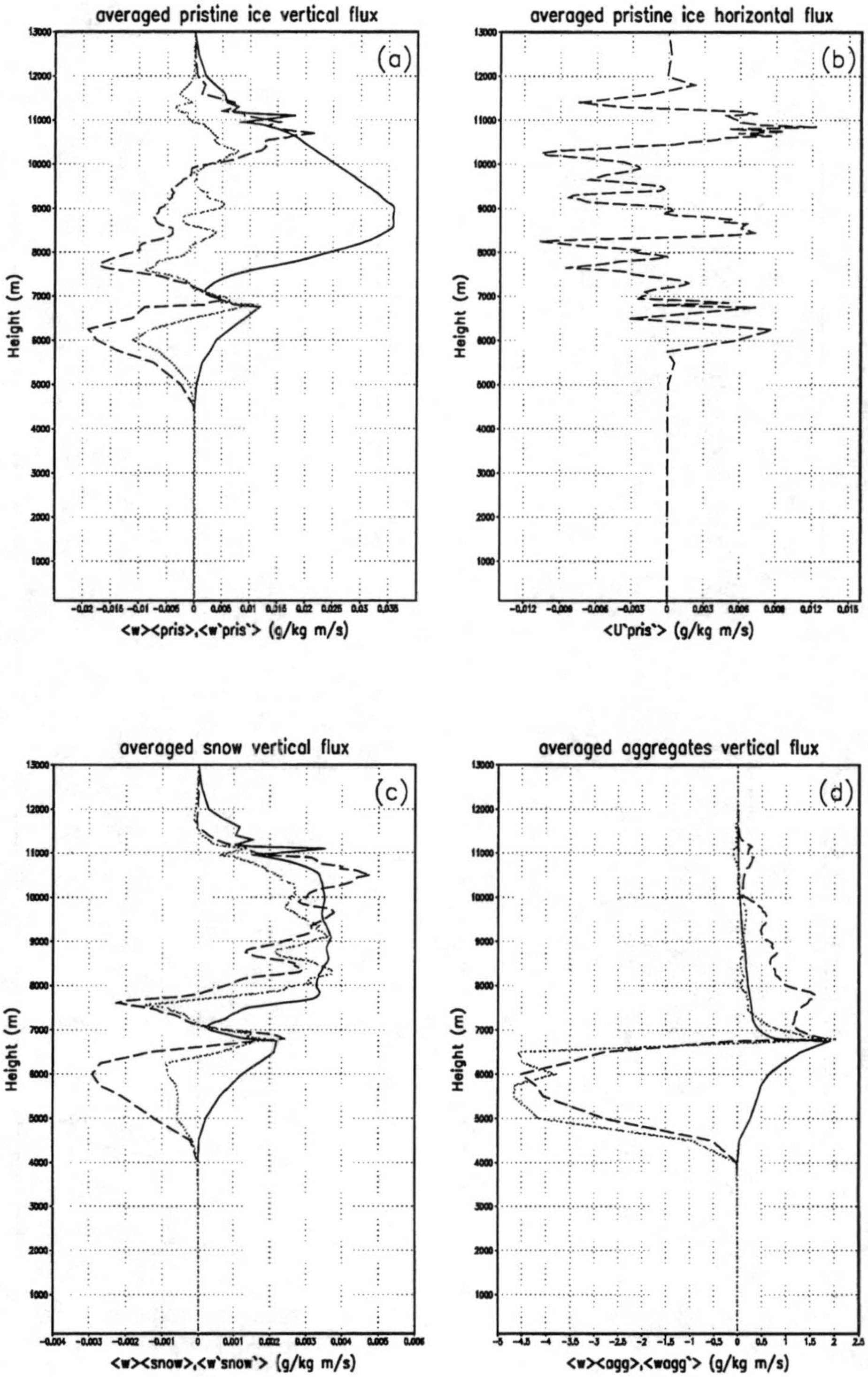

Figure 5.24: 2D simulation. (a) pristine ice averaged vertical flux (mean flux - solid, upward - dash, downward - dots); (b) pristine ice averaged horizontal flux (mean flux - solid, upward - dash, downward - dots); (c) snow averaged vertical flux (mean flux - solid, upward - dash, downward - dots); (d) aggregates averaged vertical flux (mean flux - solid, upward - dash, downward - dots).

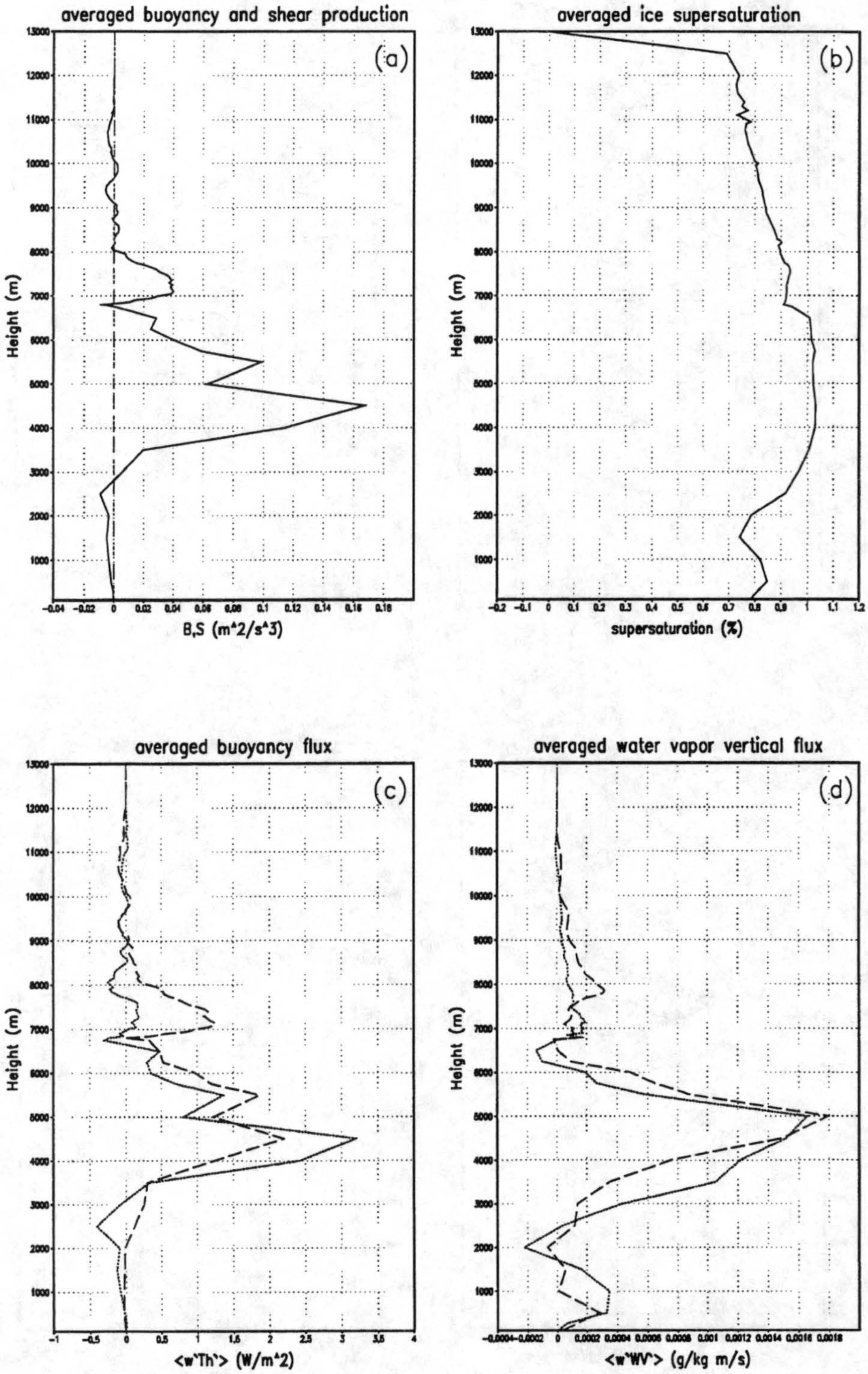

Figure 5.25: 2D simulation. (a) averaged buoyancy (solid) and shear (dash) production; (b) averaged ice supersaturation; (c) averaged buoyancy flux (upward - dash, downward - dots); (d) averaged water vapor vertical flux (upward - dash, downward - dots).

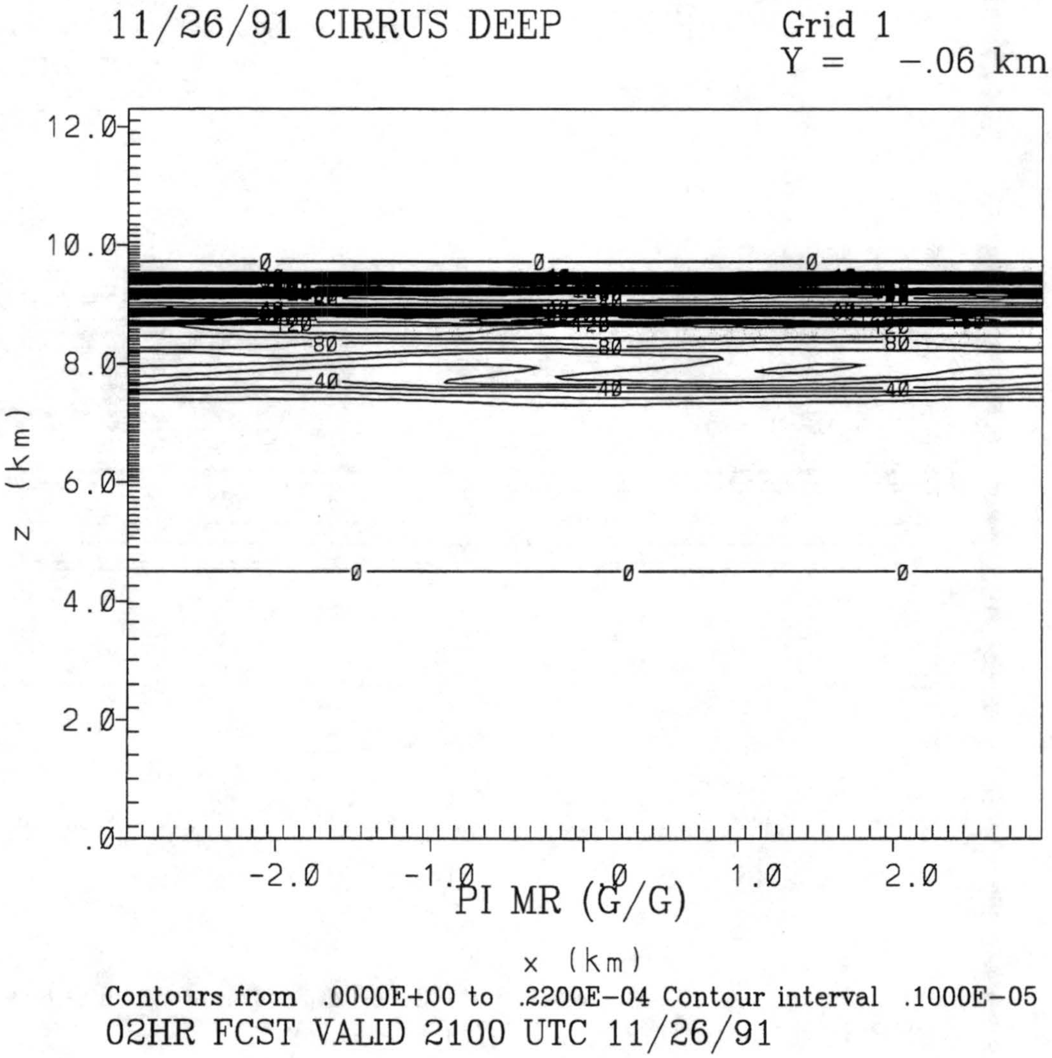

Figure 5.26: Extra–tropical simulation. Pristine ice mixing ratio.

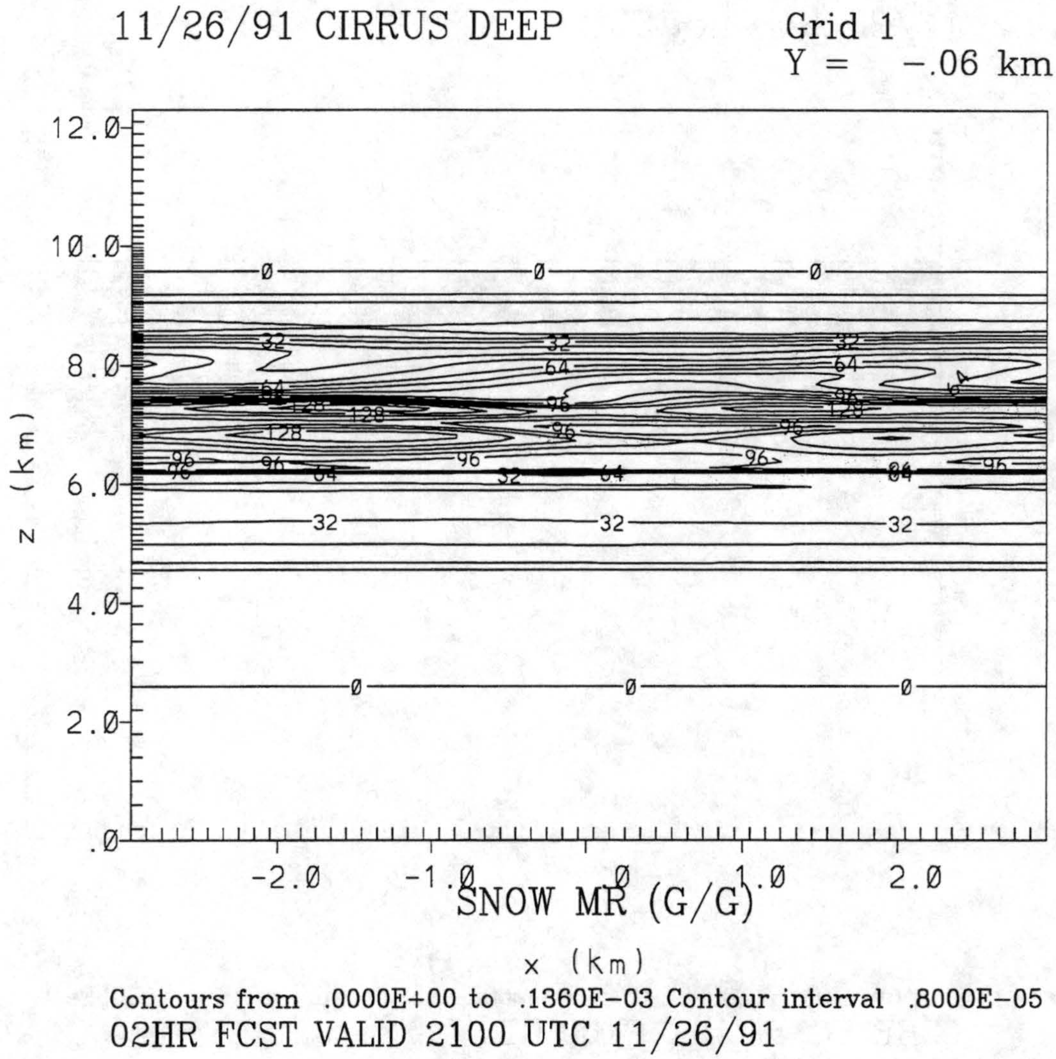

Figure 5.27: Extra–tropical simulation. Snow mixing ratio.

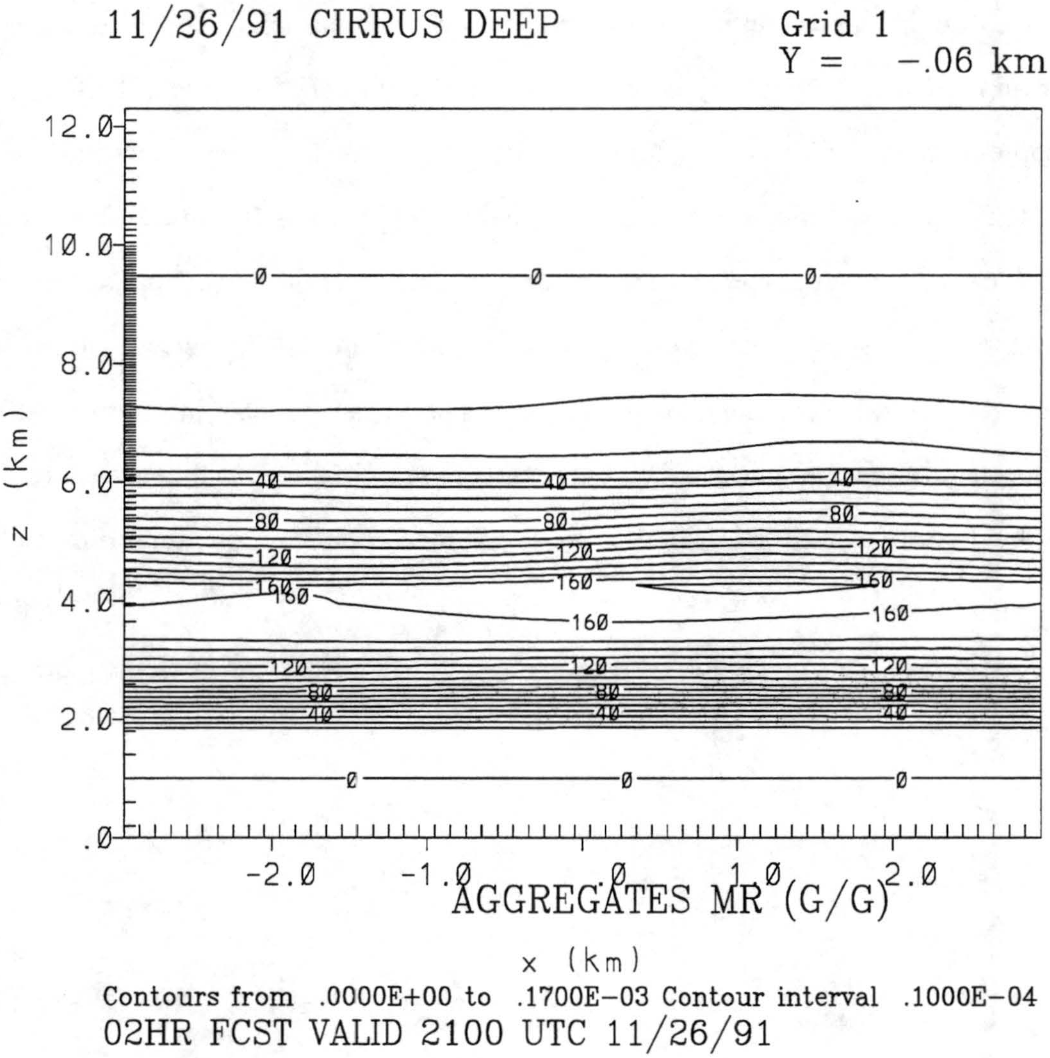

Figure 5.28: Extra–tropical simulation. Aggregates mixing ratio.

the boundary layer and stabilizes the sub–cloud layer with respect to the surface and the cloud layer with respect to the sub–cloud layer.

The presence of a drizzle flux divergence in the upper cloud layer and convergence in the sub–cloud layer reduces the heat and moisture fluxes and proves critical in the development of a stably stratified transition region. This stabilization in turn reduces the TKE production through buoyancy which has the effect of reducing the entrainment of the cloud layer. In this type of boundary layer, the TKE tends to become more intermittent and cumulus–like in the sub–cloud layer. The basic idea is that the boundary layers are strongly coupled in the presence of internal stratification.

This idea is supported by this present simulation when the two–layered cloud separated by a stable dry layer forms. Also the cumulus–like activity followed by moments of relative calmness for the sub–cloud layer as a possible interaction between the forcing due to the precipitation that tends to stabilize and turbulence that oppose this by re–mixing the sub–cloud layer is visible. The strong interaction between the top and bottom layers is visible at the moments when the TKE bursts permit penetrations of the top–cloud layer, followed by the stabilization of the bottom–cloud layer with respect to the top–cloud layer.

Chapter 6

SUMMARY AND CONCLUSION

6.1 Summary and Conclusion

Cirrus clouds have a complex microphysical structure that strongly interacts with their radiative properties, heating rates and dynamics. They have a significant effect on climate through their influence on the radiation balance and thermal equilibrium of the planet. Cirrus anvils account for most cloud cover over tropical oceans, besides marine stratocumulus, and their strong albedo effect is possibly associated with the regulation of the sea surface temperature and they produce a strong greenhouse effect. They can also induce vertical circulations due to the intense IR cooling at the top and heating at the base; also modify water concentrations in the upper troposphere and lower stratosphere.

For at least these reasons and also from a more practical point of view which concerns aviation industry and transportation safety the study and understanding of cirrus clouds has become of more and wider importance.

In this study, RAMS was used to simulate a cirrus cloud over the Western Pacific. Two distinct runs were performed: one in a three–dimensional configuration and one in a two–dimensional configuration. Because of its complexity and flexibility, RAMS was able to successfully simulate a cirrus cloud that has all the physical properties close or very close to those that were measured and/or produced by other models. And its new two–stream radiation module makes it more accurate because it takes into account individual hydrometeor species distribution parameters. In the set–up for these simulations a relatively small grid space was used: 100 m for horizontal grid spacing and as low as 50 m for most of the vertical grid spacing. Since the focus was to describe cirrus clouds, out of seven possible hydrometeors species only four were allowed: cloud droplets, pristine ice, snow and graupel along with water vapor.

The three–dimensional simulation proved realistic: it predicted a stable thick cirrus cloud with base around 8000 m and top at 11200 m. Below this layer, separated by a dry layer, another layer consisting mostly of aggregates was present. As first noted by *Stevens (1996)* these layers were coupled in the presence of internal stratification.

Mixing ratios for the ice crystals predicted by the model were in the limits of the measurements made in the tropical cirrus. Both layers showed a layered structure which is consistent with observation made with lidars.

As other studies pointed out before, it was shown that in tropical cirrus clouds the turbulence is two–dimensional in nature and the main source for producing it is due to the buoyancy term.

The heating rates, which are very important in the dynamics of a cirrus cloud and influences the microphysical processes, were within the relatively large limits measured. But as noted by *Zender and Kiehl (1994)* significant changes in heating rates can be due to small changes in the absorption properties of a given distribution of hydrometeors, which are not very well measured for the tropical cirrus and also display a large variability.

As stated before, another goal of this thesis was to determine analytical expressions for the probability distribution function (PDF) for the vertical velocity. This PDF can be used in the one–dimensional models to improve their microphysical performances. The study shows that a Gauss distribution function is a very good and simple approximation, since it requires only two measurable parameters: mean and variance of the vertical speed.

The two–dimensional run produced very similar results as the three–dimensional one, but slightly higher values. This may be due to the fact that the meridional influence near the equator is very small along with the fact that the corriolis force is neglijable. Another reason for this may be the fact that for both runs the nudging variables were obtained from a two–dimensional run of RAMS set up as a CRM.

6.2 Future research

Some of the ideas that need to be developed or take into account for future improved models is:

- The ice crystals in tropical cirrus clouds display a high geometrical complexity over a large dimensional spectra and measurements also showed the tendency for a bi–modal distribution. This is resolved in RAMS by separating the ice crystal spectra in two distinct categories (pristine ice and snow) separated by a fixed threshold value. An analytical expression to describe this feature will prove a better choice because it will eliminate the need of computing fluxes between the apparent two categories and it will be more accurate.

- A three–dimensional radiation scheme that takes into account the pronounced 3D horizontal variability that tropical cirrus clouds display. Also a better "standard" atmosphere for computing the radiative effects of CO_2 and O_3 is needed.

- Since the ocean influence on the atmosphere is very important, a coupled ocean–atmosphere model should be developed.

- Observations at cirrus levels are sparse and limited and not at all times reliable due to the limitation of the devices used in measuring ice particles characteristics especially at smaller scale. More measurements of IN and nucleation processes are needed in order to improve the model parameterization.

Bibliography

Ackerman, T.P., K.N. Liou, F.P.J. Valero and L. Pfister, 1988

Heating rates in tropical anvils, *J. Atmos. Sci.*, **45**, 1606–1623

Arkin, A. and D. Ziskin, 1994 Relationship between clouds and sea surface temperatures in the western tropical Pacific, *J. Climate*, **7**, 988-1000

Berry, E.X. and R.L. Reinhardt, 1974

Analysis of cloud drop growth by collection: Part I. Double distributions, Part II. Single initial distributions, Part III. Accretion and self–collection. Part IV. A new parameterization, *J. Atmos. Sci.*, **31**, 1814–1831, 2118–2135

Cane, M.A., 1980

On the dynamics of equatorial currents, with application to the Indian Ocean, *Deep Sea Res.*, **27**, 525–544

Cess, R.D. et al., 1990

Intercomparison and interpretation of climate feedback processes in 19 atmospheric general circulation models, *J. Geophys. Res.*, **95**, 16601–16615

Chen, C. and W.R. Cotton, 1983

Numerical experiments with a one–dimensional higher order turbulence model: Simulation of the wanganra day 33 case, *Boundary–Layer Meteorol.*, **25**, 375–404

Clark, T.L., 1977

A small–scale dynamic model using a terrain–following coordinate transformation, *J. Comput. Phys.*, **24**, 186–215

Clark, T.L. and R.D. Farley, 1984

Severe downslope windstorm calculations in two and three spatial dimensions using anelastic interactive grid nesting: A possible mechanism for gustiness, *J. Atmos. Sci.*, **41**, 329-350

Cotton, W.R. and R.A. Anthes, 1989

Storm and Cloud Dynamics, *Academic Press*, 883 pp.

Cotton, W.R., G. Tripoli, R.M. Rauber and E.A. Mulvihill, 1986

Numerical simulation of the effects of varying ice crystal nucleation rates and aggregation processes on orographic snowfall, *J. Climate Appl. Meteorol.*, **25**, 1658–1680

Cram, J.M., 1990

Numerical simulation and analysis of the propagation of a prefrontal squall line, Ph.D. dissertation, *Dep. of Atmos. Sci., Colorado State University*

Danielsen, E.F., 1982

A dehydratation mechanism for the stratosphere, *Geo. Res. Lett.*, **9**, 605–608

DeMott, P.J., M.P. Meyers and W.R. Cotton, 1994

Parameterization and impact of ice initiation processes relevant to numerical model simulations of cirrus clouds, *J. Atmos. Sci.*, **51**, 77–90

Eadie, W.J., 1971

A molecular theory of homogeneous nucleation of ice from supercooled water, Ph.D. dissertation, *Cloud Physics Lab., Univ. of Chicago*, Tech. Note **40**

Flatau, P.J., G.J. Tripoli, J. Verlinde and W.R. Cotton, 1989

The CSU–RAMS Cloud microphysical module: General Theory and Code documentation, *Dep. Atmos. Sci., Colorado State University*, Atmos. Sci. Paper No. **451**

Flatau, P.J, I. Gultepe, G. Nastrom, W.R. Cotton and A.J. Heymsfield, 1990

Cirrus clouds spectra and layers observed during FIRE and GASP projects, In *1990 conference of cloud physics, American Meteorol. Soc.*

Feingold, G., R.L. Walko, B. Stevens and W.R. Cotton, 1997

Simulations of marine stratocumulus using a new microphysical parameterization scheme, *submitted to Atmos. Res.*

Fleming, J.R. and S.K. Cox, 1974

Radiative effects of cirrus clouds, *J. Atmos. Sci.*, **31**, 2182–2188

Godfrey, J.S. and E. Lindstrom, 1988

On the heat budget of the equatorial west Pacific surface mixed layer, *J. Geophys. Res.*, **42**, 1037–1049

Griffith, T.K., S.K. Cox and R.G. Knollenberg, 1980

Infrared radiative properties of tropical cirrus clouds inferred from aircraft measurements, *J. Atmos. Sci.*, **37**, 1077-1087

Harrington, J.Y., 1994

Parameterization of ice crystal conversion processes in cirrus clouds using double–moment basis functions, *Dep. Atmos. Sci., Atmos. Sci., Colorado State University*, Atmos. Sci. Paper No. **554**

Harrington, J.Y., M.P. Meyers, R.L. Walko and W.R. Cotton, 1995

Parameterization of ice crystal conversion processes in cirrus clouds using double–moment basis functions. Part I: Basic formulation and one–dimensional tests, *J. Atmos. Sci.*, **52**, 4344–4366

Harrington, J.Y., 1997

The effects of radiative properties and microphysical processes on simulated warm and transition season arctic stratus, *Dep. Atmos. Sci., Colorado State University*, Atmos. Sci. Paper No. **637**

Heckman, S.T., 1991

Numerical simulations of cirrus clouds – FIRE case study and sensitivity analysis, *Dep. Atmos. Sci., Atmos. Sci., Colorado State University*, Atmos. Sci. Paper No. **483**

Heckman, S.T. and W.R. Cotton, 1993

Mesoscale numerical simulation of cirrus clouds – FIRE case study and sensitivity analysis, *Mon. Wea. Rev.*, **121**, 2264–2284

Heymsfield, A.J., 1972

Ice crystals terminal velocities, *J. Atmos. Sci.*, **29**, 1348–1357

Heymsfield, A.J., 1975

Cirrus uncinus generating cells and the evolution of cirriform clouds. Part I: Aircraft observations of the growth of the ice phase, *J. Atmos. Sci.*, **32**, 799–808

Heymsfield, A.J. and G.M. McFarquhar, 1996

High albedos of cirrus in the tropical pacific warm pool: Microphysical interpretation from CEPEX and from Kwajalein, Marshall islands, *J. Atmos. Sci.*, **53**, 2424-2451

Heymsfield, A.J. and L.N. Miloshevich, 1991

Limit to greenhouse warming?, *Nature*, **351**, 14–15

Heymsfield, A.J. and R.G. Knollenberg, 1972

Properties of cirrus generating cells, *J. Atmos. Sci.*, **29**, 1358–1366

Heymsfield, A.J. and C.M.R. Platt, 1984

A parameterization of the particle spectrum of ice clouds in terms of ambient temperature and the ice water content, *J. Atmos. Sci.*, **41**, 846–855

Jensen, E.J., O.B. Toon, D.L. Westphal, S. Kinne and A.J. Heymsfield, 1994

Microphysical modeling of cirrus 1. Comparison with 1986 FIRE IFO measurements, 2. Sensitivity studies, *J. Geophys. Res.*, **99**, 10421–10454

Kosovic, B., 1996

Sub–grid modeling for the large–eddy simulation of stably stratified boundary layers, *Department of Aerospace Engineering Sciences, Colorado State University*

Krueger, S.K., D. Gregory, M.W. Moncrieff, J.L. Redelsperger and W.K. Tao, 1996

GEWEX Cloud systems study working group 4: First Cloud–Resolving Model intercomparison project. Case 2, *working manuscript*

Lilly,D.K. ,1988

Cirrus outflow dynamics, *J. Atmos. Sci.*, **45**, 1594–1605

Liou, K., 1986

Influence of cirrus clouds on weather and climate processes: A global perspective, *Mon. Wea. Rev.*, **114**, 1167–1199

Mahrer,Y. and R.A. Pielke, 1977

A numerical study of the airflow over irregular terrain, *Beitr. Phys. Atmos.*, **50**, 98–113

McFarquhar, G.M. and A.J. Heymsfield, 1996a

Microphysical characteristics of three anvils sampled during the Central Equatorial Pacific Experiment, *J. Atmos. Sci.*, **53**, 2401–2423

McFarquhar, G.M. and A.J. Heymsfield, 1996b

Parameterization of tropical cirrus ice crystal size distributions and implications for radiative transfer: Results from CEPEX, *submitted to J. Atmos. Sci.*

Meyers, M.P., R.L. Walko and J.Y. Harrington, 1997

New RAMS cloud microphysics parameterization. Part II: The two moment scheme, *Atmos. Res.*, **45**, 3–39

Meyers, M.P., P.J. DeMott and W.R. Cotton, 1992

New primary ice nucleation parameterization in an explicit cloud model, *J. Appl. Meteorol.*, **31**, 708–721

Mitchell, L.D., 1997

Parameterization of the Mie extinction and absorption coefficients: A process oriented approach, *submitted to Applied Optics*

Mitchell, L.D., A. Macke and Y. Liu, 1996

Modeling cirrus clouds. Part II: Treatment of radiative properties, *J. Atmos. Sci.*, **53**, 2967–2988

Mitchell, L.D. and W.P. Arnott, 1994

A model predicting the evolution of ice particle size spectra and radiative properties of cirrus clouds. Part II: Dependence of absorption and extinction on ice crystal morphology, *J. Atmos. Sci.*, **51**, 817–832

Moncrieff, M.W., D. Gregory, S.K. Krueger, J.L. Redelsperger and W.T. Tao, 1996

GCSS Working Group on Precipitating Convective Cloud Systems: Cloud Resolving Model Intercomparison. Precipitating cloud systems in TOGA COARE: Overview, *working manuscript*

Petch, J.C., G.C. Craig and K.P. Shine, 1997

A comparison of two bulk microphysical schemes and their effects on radiative transfer using a single-column model, *Q. J. R. Meteorol. Soc.*, **123**, 1561–1580

Platt, C.M.R., S.A. Young, P.J. Manson, G.R. Patterson, S.C. Marsden, R.T. Austin and J.H. Churnside, 1997

The optical properties of equatorial cirrus from observations in the ARM Pilot Radiation Observation Experiment, *submitted to J. Atmos. Sci.*

Platt, C.M.R., 1978

Lidar backscatter from horizontal ice crystals plates, *J. Atmos. Sci.*, **17**, 482–488

Pueschel, R.F., D.A. Allen, C. Black, S. Faisant, G.V. Ferry, S.D. Howard, J.M. Livingston, J. Redemann, C.E. Sorenson and S. Verma, 1995

Condensed water in tropical cyclone Oliver, 8 February 1993, *Atmos. Res.*, **38**, 297–313

Prabhakara, C., J.–M. Yoo, G. Dalu and D.P Kratz, 1991

Optically thin cirrus clouds over oceans and possible impact on sea surface temperature of Warm Pool in Western Pacific. *NASA Technical Memorandum, No.* **104550**, *Goddard Space Flight Center, Greenbelt, MD*

Quante, M., 1989 Flugzeugmessungen der Turbulenzstruktur in Cirruswolken. technical Report No. **65**, *Institut fur Geophysik und Meteorologie der Universitat zu Koln*

Ramanathan, V. and W. Collins, 1991

Thermodynamic regulation of ocean warming by cirrus clouds deduced from observations of the 1987 *El Niño*, *Nature*, **351**, 27–32

Ramanathan, V., E.J. Pitcher, R.C. Malone and M.L. Blackmon, 1983

The response of a spectral general circulation model to refinements in radiative processes, *J. Atmos. Sci.*, **40**, 605–621

Ramaswamy, V. and V. Ramanathan, 1989

Solar absorption by cirrus clouds and the maintenance of the tropical upper troposphere thermal structure, *J. Atmos. Sci.*, **46**, 2293–2310

Reisner, J., R.M. Rasmussen and R.T. Bruintjes, 1996

Explicit forecasting of Supercooled Liquid Water in winter storm using a mesoscale model, *Q. J. R. Meteorol. Soc.*

Reynolds, D.W., T.H. Vonder Haar and S.K. Cox, 1975

The effect of solar radiation absorption in the tropical troposphere, *J. Appl. Meteorol.*, **14**, 433-443

Roeckner, E., 1988

Cloud–radiation feedbacks in a climate model, *Atmos. Res.*, **21**, 293–303

Roewe, D. and K.N. Liou, 1978

Influence of cirrus clouds on the infrared cooling rate in the troposphere and lower stratosphere, *J. Appl. Meteorol.*, **17**, 92–106

Slingo, A. and H.M. Schrecker, 1982

On the shortwave properties of stratiform water clouds, *Q. J. R. Meteorol. Soc.*, **108**, 407–426

Stackhouse, P.W. and G.L. Stephens, 1991

A theoretical and observational study of the radiative properties of cirrus: Results from FIRE 1986, *J. Atmos. Sci.*, **48**, 2044–2059

Starr, D.O'C. and S.K. Cox, 1985

Cirrus clouds. Part I: A cirrus cloud model, Part II: Numerical experiments on the formation and maintenance of cirrus, *J. Atmos. Sci.*, **42**, 2663–2694

Stephens, G.L., S. Tsay, P.W. Stackhouse and P.J. Flatau, 1990

The relevance of the microphysical and radiative properties of cirrus clouds to the climate and climatic feedback, *J. Atmos. Sci.*, **47**, 1742–1753

Stephens, G.L. and T.J. Greenwald, 1991

The earth's radiation budget and its relation to atmospheric hydrology 2. Observations of clouds effects, *J. Geophys. Res.*, **96**, 15325–15340

Stevens, B., 1996

On the dynamics of precipitating stratocumulus, *Dep. Atmos. Sci., Colorado State University*, Atmos. Sci. Paper No. **618**

Stevens, B., W.R. Cotton and G. Feingold, 1997

A critique of one– and two–dimensional models of boundary layer clouds with a binned representations of drop microphysics, *submitted to J. Atmos. Sci.*

Toon, O.B., R.P. Turco, J. Jordan, J. Goodman and G. Ferry, 1989

Physical processes in polar stratospheric ice clouds, *J. Geophys. Res.*, **94**, 11359–11375

Tripoli, G.J. and W.R. Cotton, 1980

A numerical investigation of several factors leading to the observed variable intensity of deep convection over South Florida, *J. Appl. Met.*, **19**, 1037–1063

Tripoli, G.J. and W.R. Cotton, 1982

The Colorado State University three–dimensional cloud/mesoscale model–1982. Part I: General theoretical framework and sensitivity experiments, *J. Res. Atmos*, **16**, 185–220

Tripoli, G.J. and W.R. Cotton, 1989

Numerical study of an observed orogenic mesoscale convective system. Part I: Simulated genesis and comparison with observations, *Mon. Wea. Rev.*, **117**, 273–304

Verlinde, J., P.J. Flatau and W.R. Cotton, 1990

Analytical solutions to the collection growth equation: Comparison with approximate methods and application to cloud microphysics parameterization schemes, *J. Atmos. Sci.*, **47**, 2871–2880

Walko, R.L., W.R. Cotton, M.P. Meyers and J.Y. Harrington, 1995

New RAMS cloud microphysics parameterization. Part I: The single–moment scheme, *Atmos. Res.*, **38**, 29–62

Webster, P.J. and R. Lukas, 1992

TOGA COARE: The Coupled Ocean–Atmosphere Response Experiment, *Bull. Amer. Meteorol. Soc.*, **73**, 1377–1416

Westphal, D.L., S. Kinne, J.M. Alvarez, S.G. Benjamin, W.L. Eberhard, A.J. heymsfield, R.A. Kropfli, G.G. Mace, S.Y. Matrosov, S.H. Melfi, P. Minnis, P. Pilewskie, J.B. Snider, B.J. Soden, D.O'C. Starr, T.A. Uttal and D.F. Young, 1996

Initialization and validation of a simulation of cirrus using FIRE-II data, *J. Atmos. Sci.*, **53**, 3397–3429

Zender, C.S. and J.T. Kiehl, 1994

Radiative sensitivities of tropical anvils to small ice crystals, *J. Geophys. Res.*, **99**, 25869–25880